



Original Article



Application of bridge information modelling using laser scanning for static and dynamic analysis with concrete damage plasticity

Welington Vital^a, Ramon Silva^{a,1,*}, Marcus V.G. de Moraes^{b,1}, Brunno Emidio Sobrinho^a, Rodrigo Pereira^{c,1}, Francisco Evangelista Jr.^{a,1}

^a Department of Civil and Environmental Engineering, Graduation Program in Structural Engineering of the University of Brasilia, SG-12 Building, Darcy Ribeiro Campus, Brasilia, Brazil

^b Department of Mechanical Engineering, University of Brasilia, Campus Darcy Ribeiro, Brasilia, Distrito Federal, Brazil

^c Department of Civil Engineering, University State of Minas Gerais, Pope John Paul II Highway, 4143, Ed. Minas - 8th Floor, Belo Horizonte 31630-900, Brazil

ARTICLE INFO

Keywords:

BrIM
Terrestrial Laser Scanning
Photogrammetry
Concrete Damage Plasticity
Bridge

ABSTRACT

A new proposal has been applied using Bridge Information Modeling associated to Terrestrial Laser Scanning TLS and photogrammetry to obtain the digital model of an existing bridge. For the laser scanning process. Thus, it was also possible to identify the pathologies and damages in the concrete of the bridge. Furthermore, it was shown how geo-information with remote sensing using the station Trimble SX 10 can be applied in area of bridge projects with less time and lower cost, in relationship to a conventional survey Asbuilt with manual survey in field. One of the innovations of this paper was to obtain the digital model of the bridge by integration of TLS and photogrammetry to obtain the 3D digital model. The new methodology consisted of acquisition of the bridge scenes through points previously implanted, making the polygonal contour of the entire bridge. Furthermore, the execution of the field survey from georeferenced points to capture the scenes during the sweep with TLS facilitated the refinement and, consequently, it was possible to obtain the digital model with the concrete damage. It was also possible to perform a complex nonlinear analysis with Finite Element with the digital model of the bridge. Therefore, it was applied a reverse analysis of the strength of the structure using the Concrete Damage Plasticity Model using ABAQUS software. Two numerical analyses were performed on the bridge; one considering only the static behavior of the bridge and another considering the dynamic behavior. In the static analysis, the behavior of the dapped-end beam of the bridge, was investigated. On the other hand, in the dynamic evaluation, the natural frequency and damping ratio for bridges with Dapped-end beams was obtained in ABAQUS through Rayleigh damping and compared with the technical literature, which presented satisfactory results.

1. Introduction

The Brazil instituted the National Department of Transport Infrastructure (DNIT), to be the public agency responsible to restructure the

modes of transport in Brazil. DNIT is also responsible for the maintenance, expansion, construction, inspection, and preparation of technical studies to solve problems related to the federal road system. The agency makes the management of more than 8 thousand Special Engineering

Abbreviations: E_c , Modulus of elasticity for concrete, MPa; p , Hydrostatic pressure stress; q , Von Mises-equivalent effective stress; ϵ , Eccentricity of the plastic potential surface; μ , Viscosity parameter; E_s , Modulus of elasticity of tensile longitudinal reinforcement, MPa; E_0 , Initial Undamaged modulus of the material; f_{cm} , Average Strength of concrete; f_y , Steel yielding strength, MPa; f_u , Ultimate stress; f_{b0}/f_{c0} , Relationship between biaxial compression stress and uniaxial compression; K_c , Ratio of second stress invariants on tensile and compressive meridians; ϵ_{sh}/ϵ_u , Steel strain that corresponds to onset of hardening/ultimate strain; DNIT, National Department of Transport Infrastructure; SES, Special Engineering Structures; PROARTE, Program for Maintenance and Rehabilitation of the Large Structures; BrIM, Bridge Information Modeling; AWP, Aerial Work Platforms; TLS, Terrestrial Laser Scanner; UAV, Unmanned Aerial Vehicle; CDPM, Concrete Damage Plasticity Model; GNSS, Global Navigation Satellite System; UTM, Universal Transverse Mercator; GCP, Ground Control Points; RTK, Real-Time Kinematic; GSD, Ground Sample Distance; DTM, Digital Terrain Models; GERBER, Dapped-end beams.

* Corresponding authors.

E-mail addresses: welington.silva@unb.br (W. Vital), ramon.silva@unb.br (R. Silva), mvmoraes@unb.br (M.V.G. de Moraes), fejr@unb.br (F. Evangelista).

¹ These authors contributed equally to this work.

<https://doi.org/10.1016/j.aej.2023.08.023>

Received 23 October 2022; Received in revised form 2 July 2023; Accepted 7 August 2023

1110-0168/© 2023 THE AUTHORS. Published by Elsevier BV on behalf of Faculty of Engineering, Alexandria University. This is an open access article under the CC BY-NC-ND license (<http://creativecommons.org/licenses/by-nc-nd/4.0/>).

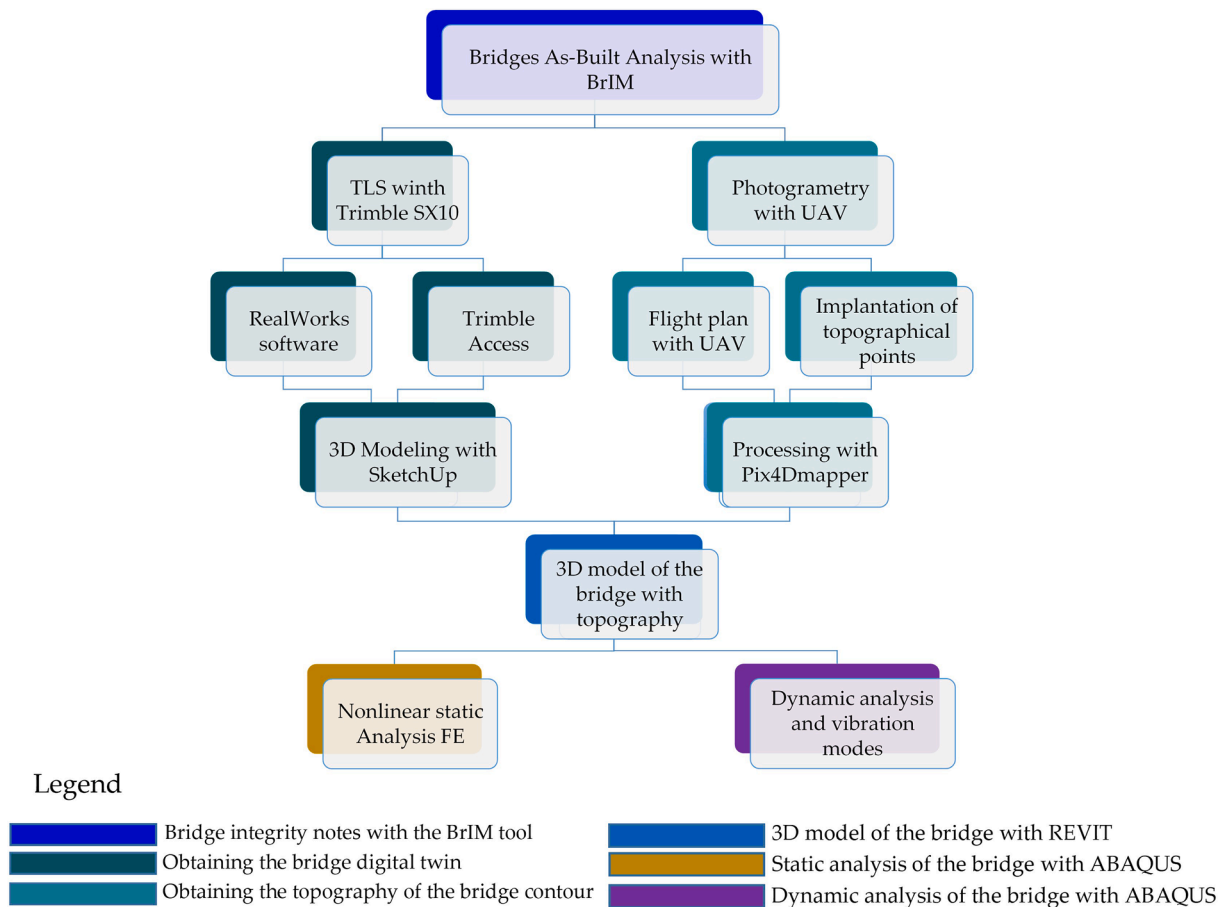


Fig. 1. Flowchart with the analyses carried out in this research.

Structures – SES (Bridges, Viaducts, Tunnels and Footbridges) [1].

Recent collapses of road bridges have led the technical–scientific community and society to reflect on the effectiveness of their management [2]. In this context, due to the high number of SES that need structural recovery, DNIT created in 2017 the Program for Maintenance and Rehabilitation of the Large Structures, called - PROARTE, which became responsible for manage maintenance and rehabilitation of these large structures. Within the scope of PROARTE, the Bridge Information Modeling – BrIM methodology was implemented, which establishes the technical criteria for the development of preliminary design of bridge on the BrIM platform for bridge rehabilitation works [3–15]. For the purpose of applying BrIM, an inspection is initially carried out at the SES to determine the degree of degradation of the structure, to determine a management note for the structure and, then, define a prioritization rule of which bridge will be reinforced first, based on the standard ABNT NBR 9452 (2019) [16], DNIT-010 standard [17], and the ABNT NBR 7188 (2013) [18].

Photogrammetry and laser scanning are solutions that can be integrated and enable the representation of existing bridge elements in three-dimensional digital models [19]. On the other hand, in inspections of bridges and viaducts, design engineers face difficulties in accessing important points of the structure, impairing the collection of essential data for the characterization of geometric elements of the SES as well as in obtaining the measurements of the observed pathologies in inspections. That in most cases to have access to the structural elements of the superstructure requires several special equipment that have a high cost for mobilization and execution.

Koch et al. [20] presented current achievements, open challenges in vision-based inspection of large concrete structures and vision-based 3D reconstruction and as-built spatial modeling of concrete civil

infrastructure with focus in set on structural member recognition as well as on concrete damage detection and assessment exemplified for concrete columns.

McGuire et al. [21] presented a method and prototype implementation for tracking and assessing the structural condition of bridges using BIM. In the proposed method, an inspector uses a custom software add-in, developed by the authors, to capture information on damage type, amount, severity, and location gathered during bridge inspection. Next, a custom tool in Microsoft Excel evaluates the structural performance and provides simplified load ratings of the inspected bridge. The proposed method was validated through field testing on a case study bridge. Findings from this study suggested that BIM can effectively facilitate the inspection and evaluation of bridges.

Riveiro et al. [22] presented a new method for fully automated point cloud segmentation of masonry arch bridges. The method efficiently creates segmented, spatially related and organized point clouds, which each contain therelevant geometric data for a particular component (pier, arch, spandrel wall, etc.) of the structure. The method was validated using a representative sample of masonry arch bridges. The results demonstrate that this tool can provide data for further structural operations without requiring neither training in laser scanning technology nor high-performance computers for such data processing.

Sedek and Serwa [23] applied laser remote sensing data of asbuilt model, with BrIM (Bridge Information Model) for a constructed bridge. An experimental work was carried out to confirm the planned method for monitoring the structural defects through a case study was implemented in the design and inspection data in the Jacques Cartier Bridge in Canada. The outcomes demonstrated that the existing technique can be employed to sense the defected elements or structure imprecision fast and accurately.



Fig. 2. Dom Pedro II steel bridge with 237 m of span with a height of 86 m over San Francisco River in Brazil.

In general, the researchers found in the literature only use the TLS and BIM to obtain a digital model or even to do a simplified analysis of the model obtained. Therefore, the objective of this paper is perform a Terrestrial Laser Scanning -TLS and photogrammetry on the bridge over the Pianco River to obtain the point clouds and a 3D model that represent the existing structure with concrete damage. In addition, is perform a nonlinear Finite Element modeling using ABAQUS for obtain the natural frequencies and mode shapes of the bridge, as well as the stress concentrations in the structural elements using Concrete Damage Plasticity Model. With these results, it is possible to define a better solution for rehabilitation project of the bridge. The Fig. 1 shows the research flowchart.

2. Materials and methods

2.1. Typologies of bridges indicated for TLS and photogrammetry

When the design engineer has easy access to bridge elements and does not need special equipment to carry out the inspection and access all bridge elements is possible to carry out the measurements of the

sections with the use of a simple tape measure for obtaining of AsBuilt. In this case, the TLS and photogrammetry still have a cost that does not justify their application in the survey of AsBuilt. In relation to field survey with a manual tape measure, without use of equipment to access bridge elements. However, the purpose of this paper is to make the TLS and photogrammetry in bridge with difficult access to the structural elements. Since that, the realization of the conventional survey using a simple tape measure would require several special equipment, whose cost would be high compared to TLS and photogrammetry. Thus, the Figs. 2 and 3 show three examples of bridges that have difficult access to structural elements to perform AsBuilt using a manual tape measure.

This paper aims to overcome the standard methodologies for pavement, beams, column cap, column, joints and girder inspections of a bridge, which require the use of By-bridge equipment (see Fig. 4), Aerial Work Platforms (AWP) or ropes. These methodologies have several limits and risks, especially in difficult to access areas or with obstacles [24,25].

2.2. Terrestrial laser scanning in bridge design application

A detailed review of the literature from the last decades showed that TLS has been widely used in geosciences, infrastructure monitoring, structural assessment with damage detection, and As-Built survey of architectural buildings, among other topics in engineering and medicine. Indeed, TLS allows the accurate and fast acquisition of millions of points that represent the scanned structure in a digital file composed by a cloud of points [5,26,27]. The Trimble RealWork software is specifically designed for point cloud processing and analysis.

2.3. Use of photogrammetry to obtain the digital terrain model in bridge

Nowadays, with the development of digital photography and the digital treatment of the image with photogrammetry, a method



Fig. 3. (a) The Biggest cable-stayed Bridge in Brazil pass over the Rio Negro, has a central span of 400 m with a mast of 185.00 m of high; (b) Felipe Guerra Bridge over the Piranhas/Açu River with 585 m of extension with 2 main beams of section variable type parabolic.

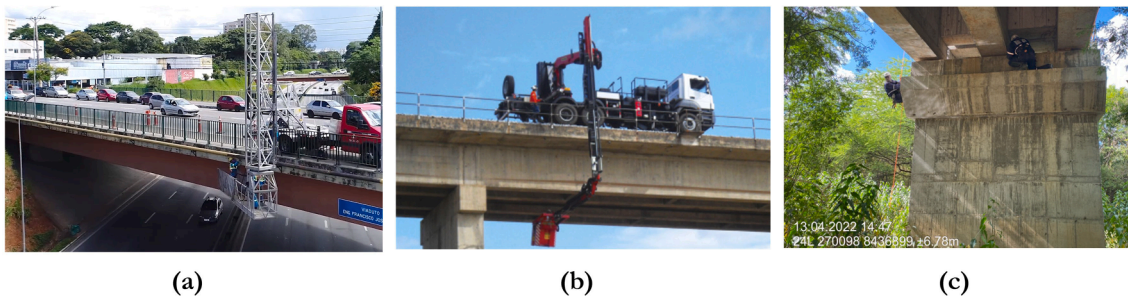


Fig. 4. Bridge inspection. (a) and (b) Inspection of the bridge using special equipment coupled to the munck truck; (c) Inspection of the bridge using rappelling equipment using ropes to access the columns.

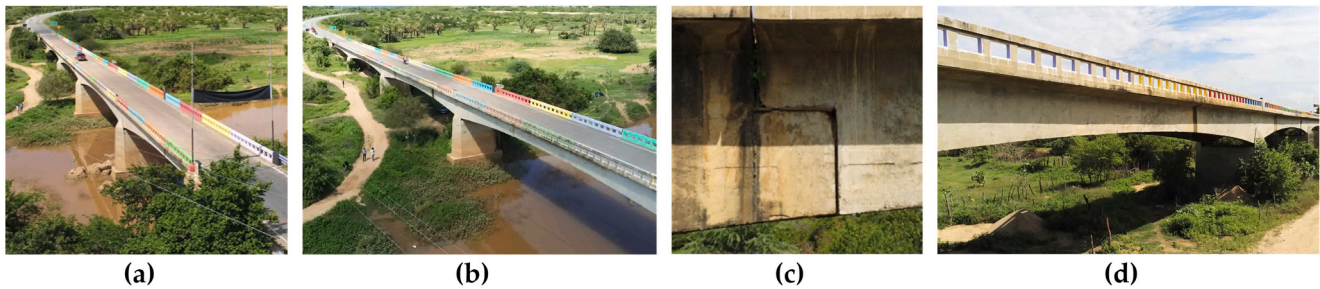


Fig. 5. Details of the bridge over the Pianco River. (a) and (b) General view of the bridge; (c) half-joint or dapped-end beam; (d) Beam with parabolic section.

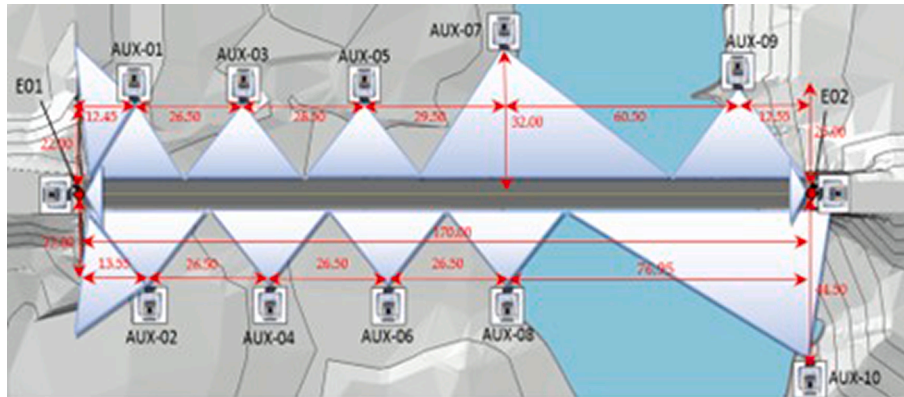


Fig. 6. Total station positions along the bridge to scanning with TLS of the bridge elements with measurements in meters.

developed at the beginning of the 20th century and presents new fields of application with advantages over traditional methods of obtaining the Digital Terrain Model [28,29].

The field of application of this technique within civil engineering is focused on mainly for aerial surveying in obtaining of the contour lines [28]. Photogrammetric models use the principle of triangulation to identify points between two different images and triangulate them back to a single point of view [29].

Abdelwahab [30] proposed the creation of the digital terrain model (DTM) included two components, the surface model and satellite images. A surface model was created using the available topographic contours maps which created a mesh looking image that defines the 3D geometry of the site. Then, to make the DTM more realistic, satellite images were superimposed on the 3D surface creating a realistic earth surface applied to bridge project.

3. Field surveys and processing

3.1. Work methodology in the survey with TLS

Sketches with hand-drawn photos may not provide comprehensive information or may miss small important details of the project. The Creation of a digital model of a bridge solves this problem as the digital model is an exact replica of reality that can be shared between engineers, bridge design specialists and construction teams, using TLS this process makes it more accurate, secure is fast. The bridge investigated with TLS in this paper has a typology similar the bridge shown in Fig. 3 in the item (b), which, superstructure is composed of two beams in variable section parabolic type in reinforced concrete (See Fig. 5). The bridge over the Pianco River have 5 spans of 34.00 m, with 170.00 m length. The cross-section of the bridge has two lanes of 3.00 m of width and two guardrails of 0.20 m of thickness and 0.90 m high, the total width of the bridge is 6.40 m.

To carry out the TLS, the work methodology consists in the implementation of the polygonal points, starting with the bridge abutments.

After, defining the points at abutment E01 and abutment E02, located at the top of the bridge, auxiliary points were launched in strategic locations, as shown in Fig. 6 with total station measurements in cm. The auxiliary points served as a basis for parking the Trimble® SX10 total station to scan the underside of the structure, scanning the individual already georeferenced for easy post-processing.

The points at which the total station was positioned were georeferenced through Global Navigation Satellite Systems GNSS of the dual frequency with receiver to the UTM SIRGAS 2000 coordinate system. The processing of these points was performed using the service of Precise Point Positioning (PPP) provided on the platform of the Brazilian Institute of Geography and Statistics. After the implementation of the polygonal points, the laser scanning step was started, which consists of a high precision three-dimensional survey for digital documentation purposes, resulting in a cloud of points.

This means that points were captured in a defined window area along a grid interval specified by the user, but without user intervention during scanning, everything is done automatically, and in particular no need to aim at each individual point of the structure [31]. Subsequently, to finish each scene, photos were taken using the Trimble® SX10 station itself, to obtain details of the pathologies in the structure.

3.2. TLS settings for getting the point cloud

The Trimble® SX10 robotic total station has three viewing cameras: an overview camera; another of primary division; and finally, a camera on the telescope that does the laser scanning [27,31]. In addition to these cameras, two more are attached to the total station, one to assist in fixing the robotic total station at the point of the polygonal, and another camera to locate and follow the prism during topographic survey. In this context, the execution of the implementation of TLS, was first, fixed the robotic total station Trimble® SX10 with the specific camera for recognizing the topographic point of the polygonal at the points indicated in Fig. 7.

To obtain the best precision in this paper, the superfine cloud was

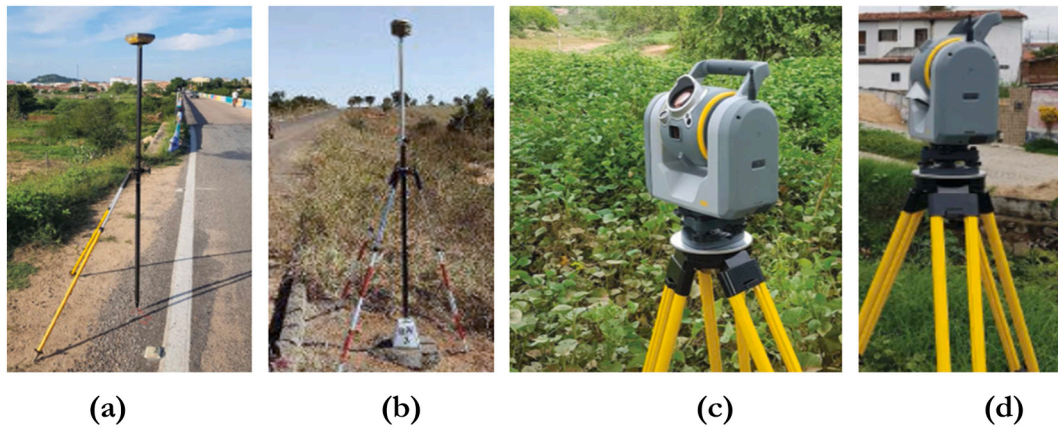


Fig. 7. Equipment used in the TLS of the bridge over the Pianco River. (a,b) Capture landmarks for georeferencing; (c-d) Trimble® SX10 Bridge Scan with TLS.

Table 1
Overview of scanning Trimble® SX10 total station with some of their technical specifications according to manufacture [23].

Trimble® SX10 Total Station	
Features	Results
Date of release	2016
Angular accuracy	1"
EDM maximum range	5500 m (prism) 800 m (non prism)
EDM accuracy (prism)	1 mm + 1.5 ppm
EDM accuracy (non-prism)	2 mm + 1.5 ppm
Imaging	
Number and kind of cameras	overview + primary + coaxial
Resolution	5 Megapixel
Frame rate	up to 15 Hz
Scanning	
Maximum rate	26,600 pts/s
Maximum range	600 m
Scanning range noise	1.5 mm @ 50 m
Additional Features	Scanning & enhanced VISION
Laser Class and Ingress Protection	Laser Class 1 M & IP55



configured in the scan of the bridge elements. In addition, chosen configuration was used to color the point cloud, as well as superimposing these images in post-processing with Trimble® RealWorks with recognition of cloud features. Another application used during point scanning was Trimble® Access, which enabled the visualization of data acquired in the field, automatically, with all colored point clouds. Thus, it was possible to ensure that all elements of the bridge structure were captured by zooming the point cloud using the tablet, connected via remote (with to 700 m away from the Trimble® SX10 total station). Table 1 shows the main Trimble SX10 total station configurations using in the survey field.

The Fig. 7 shows the Trimble® SX10 total station with the equipment for georeferencing the points, with the GNSS type GPS receivers TOPCON HIPER SR.

In the scanning point cloud processing, a segmentation was first performed, eliminating noise and separating the parts of the structure. The 3D modeling was performed from the point cloud. Which consists of creating 3D models in CAD format that can be integrated into architectural design software, with BrIM tools [32]. The 3D modeling was divided between RealWorks software, for cloud segmentation and feature extraction, and Sketchup for model creation and finishing. The RealWorks together with Sketchup have a direct link, which facilitates transfer of information in the Trimble® platform, finally, the IFC model was imported from Sketchup to REVIT®, where the 3D model was refined with the creation of families of each bridge element according to the criteria of the BrIM from PROARTE.

3.3. Application of georeferenced points to obtain of the photogrammetry

Photogrammetry was carried out on the contour of the bridge over the Pianco River to obtain the topography of the terrain, which was integrated with the TLS to acquire the As-Built of the bridge with the terrain profile. Therefore, in order to carry out photogrammetry, it was necessary, initially, to install control points that are landmarks used to increase the geographic accuracy of images obtained during aerial surveys. The Ground Control Points GCP were identified through landmarks along the terrain, inserted in the areas where the aerial survey took place. These points were used to relate the image coordinate system to the georeferenced terrain coordinate system. These control points (GCP's) were georeferenced using a dual frequency GNSS receiver with closure of the polygonal using the Trimble® SX10 total station. Thus, 40 support points were randomly deployed in the study area, with PPP processing after tracking with the TOPCON HIPER SR GNSS system through Real-Time Kinematic - RTK. The use of GCP's in aerial mapping with drones is always associated with the use of high geographic



Fig. 8. Details of the aerial survey of the topography on the bridge over the Pianco River.



Fig. 9. Using the Parrot ANAFI UAV in the photogrammetry with 180° camera gimbal.

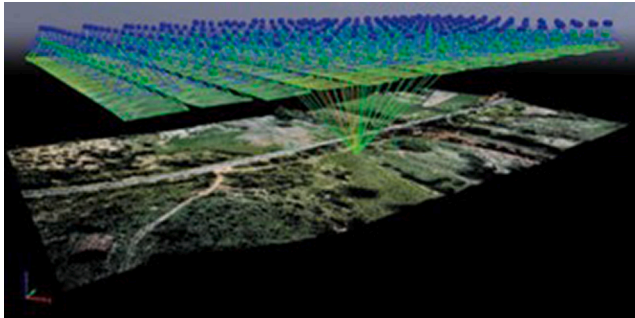


Fig. 10. Processing aerial photogrammetry with the Pix4Dmapper with duration of 13 h:29 m:08 s,

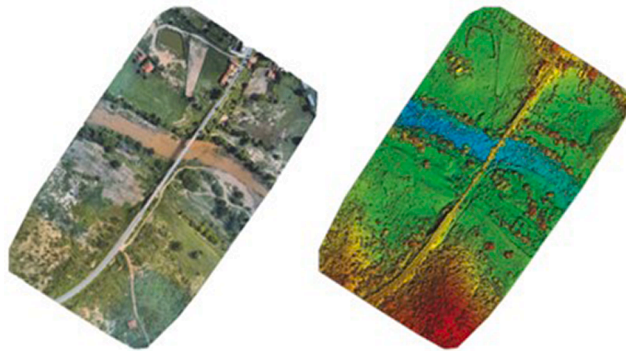


Fig. 11. Orthomosaic and the corresponding sparse Digital Surface Model DSM before densification.

precision technologies, such as Real-Time Kinematic.

The flight plan was made with the application Pix4Dcapture, with a flight height of 80.00 m and the Ground Sample Distance GSD obtained was 2.7 cm. Fig. 8 shows the details of obtaining the georeferenced points and with the position of the targets for the aerial survey, as well as the images of the Pix4Dcapture application used to process the images.

In the aerial survey, the Parrot ANAFI Work drone was used, which captures high-resolution images and 4 K videos, in addition to provide high accuracy in the mapping. The ANAFI has a key feature for bridge inspection and topographic surveying below the bridge. Fig. 9 shows an overview of the Unmanned Aerial Vehicle of the Parrot ANAFI used in the photogrammetry.

The aerial photogrammetry processing was performed in the Pix4Dmapper software, capable of processing drone images and creating orthomosaic and high-quality point clouds with accuracy as shown in Figs. 10 and 11.

In the office stage, it was started with the processing of the aerial survey images, the coordinates of the control points and the correlation with the images was entered, then a dense and orthomosaic point cloud

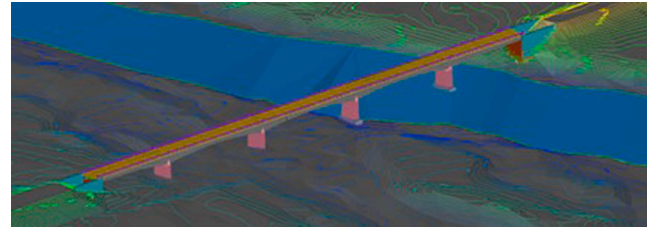


Fig. 12. Topography on the contour of the bridge obtained from the point cloud.

was generated. Subsequently, the segmentation of the point cloud was performed using Autodesk's ReCap software, and obtained a digital model of the aerial survey, which was finally exported to Autodesk's CIVIL 3D for refinement and finishing the Digital Terrain Models DTM. Fig. 12 shows the details of the DTM contours in the bridge segment.

4. Results of the TLS and photogrammetry

In order to keep the adequate safety levels in critical infrastructures such as bridges is essential to modern societies and their vital services. Reinforced concrete bridges are subject to deterioration, especially due to corrosion effects. Support Gerber are among the key components of bridges which are especially exposed to environmental actions due to their position and reduced possibility of inspection [33]. However, with the use of TLS, it was possible to identify the cracks in the Gerber of the bridge, as well as other pathologies in the concrete, shown in the Fig. 13.

The 3D SketchUp model was used to export to REVIT software and so on the parameterized families of the structural elements was developed, finishing the as-built modeling process of the bridge from TLS (see Fig. 14).

5. Numerical bridge simulation

5.1. Concrete damage plasticity model in ABAQUS

After obtaining the 3D model of the bridge in REVIT, the numerical simulation of the structural elements was performed through nonlinear analysis with Finite elements (FE) using ABAQUS. The non-linearity of concrete can be a result in a cracking process due to tensile stresses, which cause plastic stresses at the crack ends during loading. Another failure mechanism observed in concrete is failure by crushing in the compression zone. The Concrete Damaged Plasticity Model (CDPM) was designed with the aim of encompassing all the particularities of concrete.

Moreover, a consolidated approach in numerical simulations with FE in reinforced concrete is the CDPM. Derived from the Drucker-Prager criteria, which consists of a multiaxial constitutive model. The CDPM, also known as the Barcelonan model, was first introduced by Lubliner et al. [34] who presented a strategy for considering the degradation of stiffness in which the damage variables were coupled to the plastic

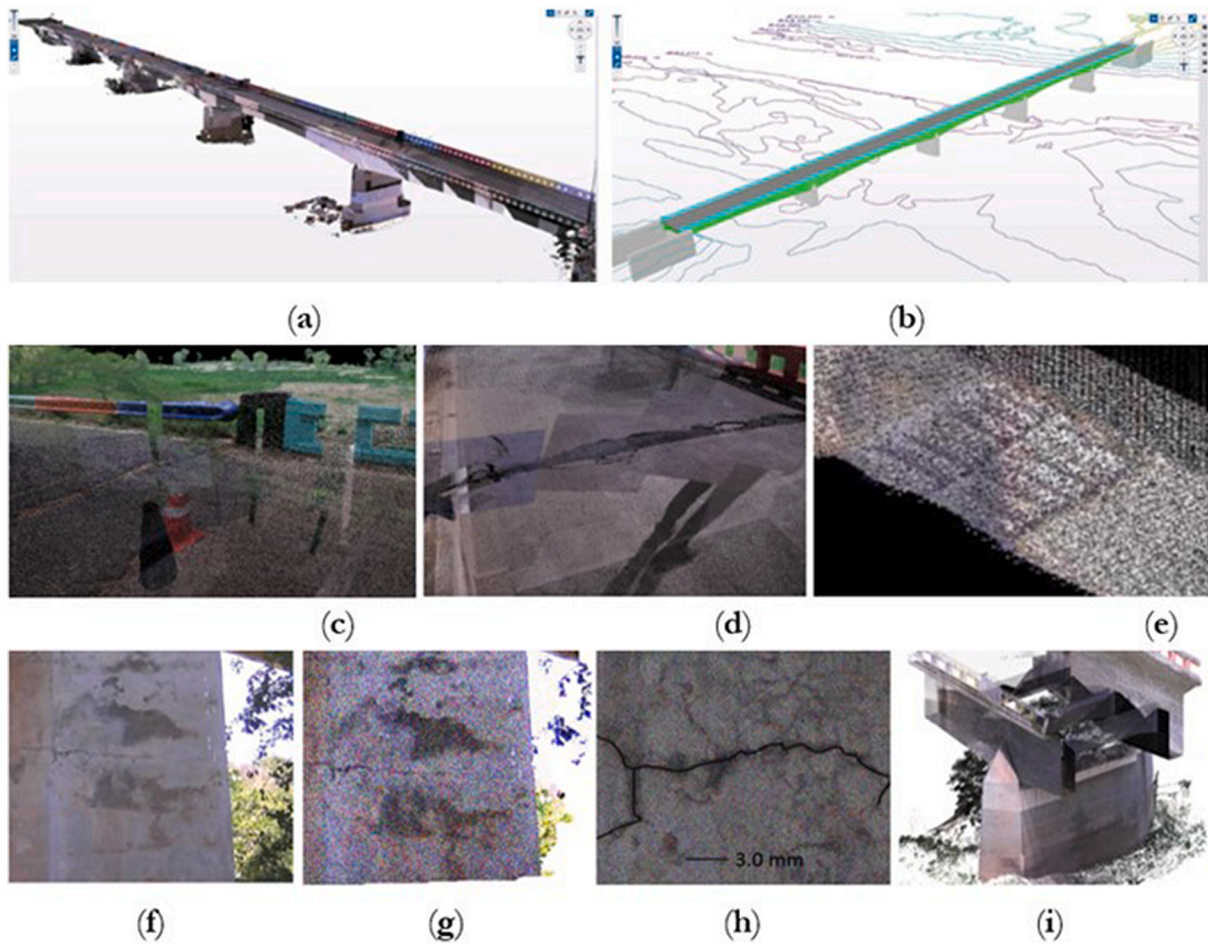


Fig. 13. Modeling results with TLS. (a) Bridge model with point cloud; (b) Bridge model in Trimble SketchUp through the point cloud; (c and d) Pathologies in expansion joints; (e) Pathologies in the beam of the bridge with exposed steel wires of the midspan of the beam; (f) to (h) Cracks on the bridge pier of the midspan; (i) Bridge isometry with cross section cut in point cloud processing.

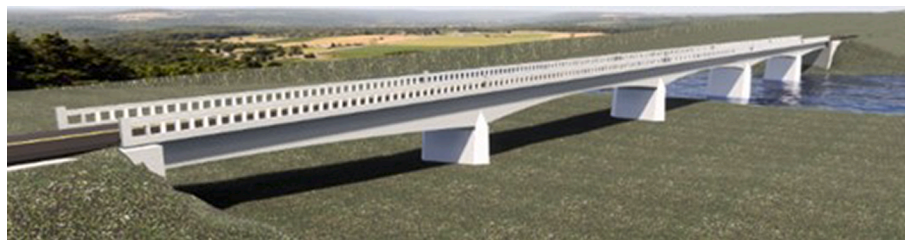


Fig. 14. 3D model of the bridge in the BrIM.

deformations in the constitutive relationships, where, the parameters used in the model were obtained from experimental results in concrete or from normalized curves in the design codes.

In the CDPM implemented in the ABAQUS software, it is defined the behavior of concrete basically dependent on five parameters (K_c , ψ , fb_0/fc_0 , ϵ , μ). First, the yield surface of the CDPM model in the plane of deflection stress is non-circular to allow for different triaxial yield stresses and compressive stresses (See Fig. 15a) [35,36]. This non-circular flow surface is governed by the plastic variable K_c . The value of K_c represents the ratio between the distance from the hydrostatic axis to the traction and compression meridian in the deviatory plane, equivalent to the ratio between the deviatory stress in uniaxial traction and compression.

Physically, this parameter K_c is interpreted as a ratio of the second invariant of stress in tension and compression for the same hydrostatic

stress. On the other hand, the value for K_c must satisfy the relationship of $0.5 \leq K_c \leq 1$ to guarantee the convexity of the surface, the value of $K_c = 2/3$ is normally recommended for the CDPM model, and the graphic form corresponds to the combination of three tangent ellipses (See Fig. 15b). However, when the parameter K_c assumes a value of $K_c = 1$, the failure surface becomes a circle, as in the Drucker-Prager criterion, which converges with the results of the multiaxial tests that showed the deviatory plane of the concrete to be almost circular in high hydrostatic pressure [37]. Likewise, the CDPM is a two-invariant plasticity model, where the yield surface is a modified Drucker-Prager force hypothesis, incorporated in the ABAQUS software library [38,39].

The 2nd plastic parameter is the dilation angle, which is defined as a frictional material with internal friction between particles, such as concrete, it is a phenomenon that causes inelastic volume variation because of plastic distortion, dilation can also be attributed to the

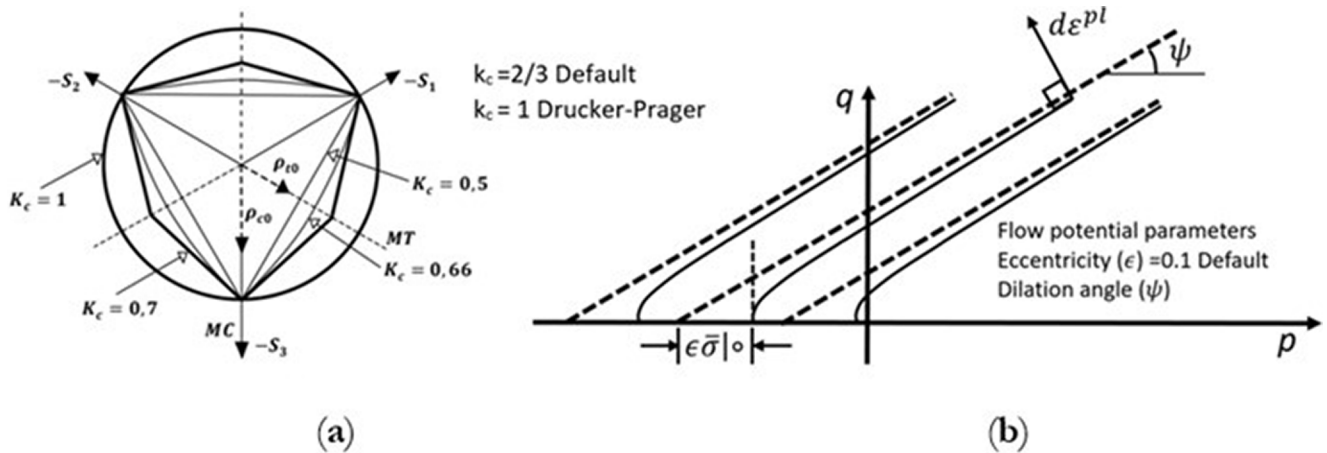


Fig. 15. Graphic interpretation of K_c values and flow potential parameters. (a) Flow surface in the deviatoric plane for the general values of K_c and (b) Hyperbolic in the meridional plane with the indication of the dilatancy angle.

Table 2
Plasticity parameters for CDPM in ABAQUS.

Parameter.	Value	Description of variables [39,49]
K_c	2/3	Coefficient that determine the shape of the deviatoric cross-section
ψ	15	dilatancy angle
f_{b0}/f_{c0}	1.16	Ratio of initial equibiaxial compressive yield stress to initial uniaxial compressive yield stress
ϵ	0.1	Eccentricity of the plastic potential
μ	0.0001	Viscosity parameter
E_c [MPa]	39,598	Young's modulus
ν	0.19	Poisson's ratio
Density [kg/m ³]	2000	Concrete density

growth of micro-cracking mechanisms that concrete undergoes during inelastic deformation [35]. The CDPM has a dilation control, that is, a volumetric expansion during shear [36]. This is an important phenomenon in plasticity in cases of concrete structures subjected to multiaxial loads. Concretes with low values of dilation angle (ψ) present brittle behavior, while high values provide concrete with high ductility Fig. 17b shows the relationship of the dilation angle with the hyperbolic

plastic potential function in the meridional plane.

The 3rd parameter used in CDPM describes the state of the material when submitted to compression, represented by the ratio between the biaxial compressive strengths at the beginning of non-linearity and the uniaxial stress (f_{b0}/f_{c0}). ABAQUS uses a standard ratio to stress ratio (f_{b0}/f_{c0}) with a value of 1.16 based on the Kupfer curve [40,41]. The 4th variable is called the eccentricity ϵ . Due to the shape of the plastic potential function in the meridional plane is hyperbolic and not circular, it is necessary to adjust this shape, through the eccentricity, which assumes a small value that expresses the rate of approximation of the hyperbola to its asymptote.

Eccentricity can be calculated in the uniaxial case as the ratio of ultimate tensile to compressive stress. As the eccentricity value increases, the curvature for the potential function increases, implying that the dilation angle increases faster the confining pressure decreases. When assuming zero eccentricity, the behavior of the CDP is similar to the Drucker - Prager criteria, that is, the surface in the meridional plane becomes a straight line. Therefore, the default value used in the technical literature is $\epsilon = 0.1$ in almost all publications [37–39,42–45].

Finally, the 5th variable, which represents the concrete viscosity μ , is not directly applied in the CDPM equations, but it is assumed that the stresses may exceed the yield surface by a certain tolerance, which is

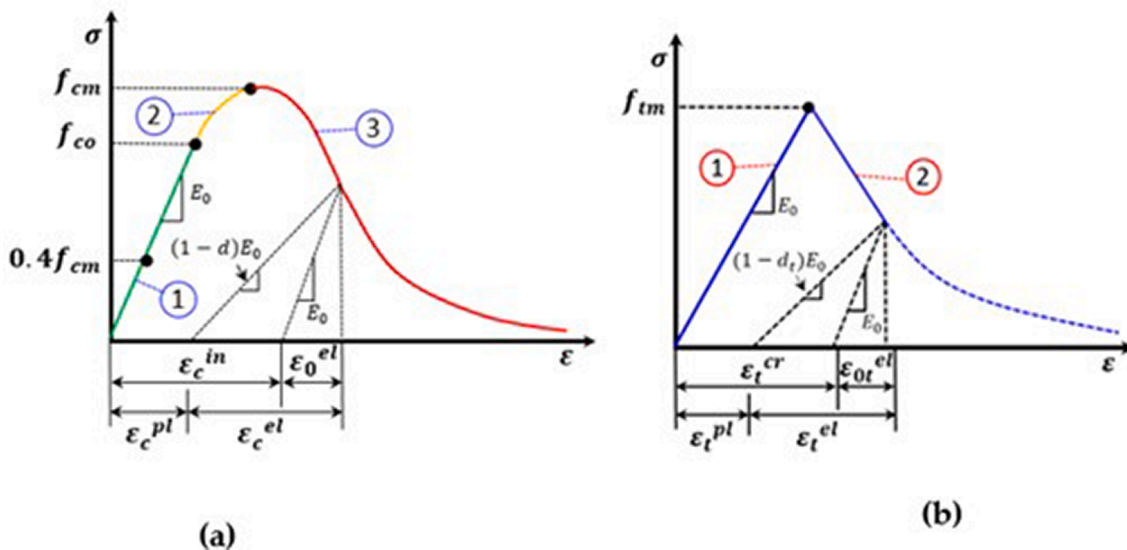


Fig. 16. Relationship between parameters in CDP model. (a) Determination of the damage variable for concrete under compression d_c . (b) Relationship of the damage variable for concrete under tension d_t .

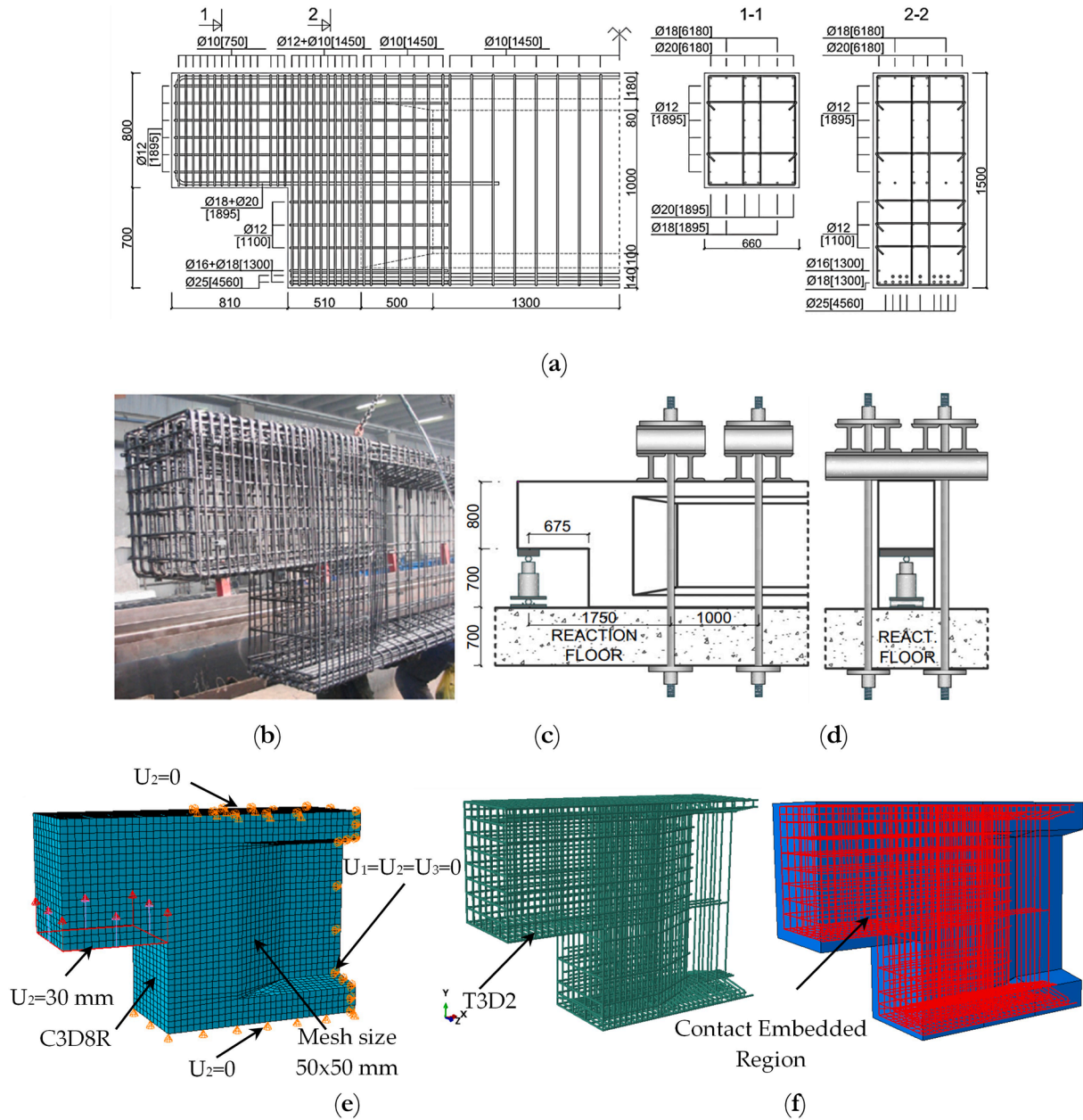


Fig. 17. Numerical simulation of dapped-end beam of Nagy-György et al. (2012) [48]. (a) Reinforcement details with dimensions in mm; (b) Reinforcement detailing of the beam; (c) and (d) Reaction floor with bars and profiles for beam testing; (e) Boundary conditions of numerical simulation; (f) Truss element used in the simulation with contact embedded region.

Table 3
Properties of the material, determined in laboratory test [48].

Diameter (mm)	f_y (N/mm ²)	f_u (N/mm ²)	ϵ_y (‰)	ϵ_u (‰)	ϵ_{ult} (‰)
10	780	922	3.60	14.90	15.50
12	522	600	2.50	23.10	24.0
16/18/20	460	600	2.20	19.90	21.10
25	440	625	2.20	18.90	20.0

determined by the viscosity. Thus, viscosity is used because of the difficulty in numerical convergence in softening. With the decrease in stiffness it is possible to allow viscoplastic regularization, the values recommended in the technical literature are between 0.0 and 0.0005 [37,45–47].

Table 2 shows the parameters of the CDPM applied in model of the half-joint beam of Nagy-György et al. (2012) [48] and also to the bridge over the Pianco River.

The CDPM model in ABAQUS also needs the definition of damage variables which are designed to model the degradation of the concrete stiffness [41]. CDPM offers a progressive material damage modeling capacity, in which the scalar damage variable varies from $d = 0 \leq d \leq 1$. In this case, $d = 0$ corresponds to a fully intact material and $d = 1$ relates to complete damage or initiation of fracturing [36,50]. The compression damage factors d_c and tension d_t , represent the rate of degradation of concrete stiffness caused by damage to the material during compression and tension, respectively, under uniaxial stress. Fig. 16 (a) and Fig. 16 (b) shows the behavior of concrete under uniaxial compressive and tension stress, respectively. Note that the graph in Fig. 16 (a), the relationship between stress and strain has three phases [51].

The details of phases are described as follow: Phase 1: in this phase, the relationship of stress–strain is denoted linear given by $\sigma_{c(1)} = E_0 \epsilon_c$. At the end of this phase registered the average strength of concrete (f_{cm}) as being $\sigma_c = 0.4f_{cm}$ according to EC2 [52]. The also according to CEB-FIP (2010) [53] defines that $E_{ci} = 10000f_{cm}^{1/3}$ with $E_0 = (0.8 + 0.20f_{cm}/88)E_{ci}$

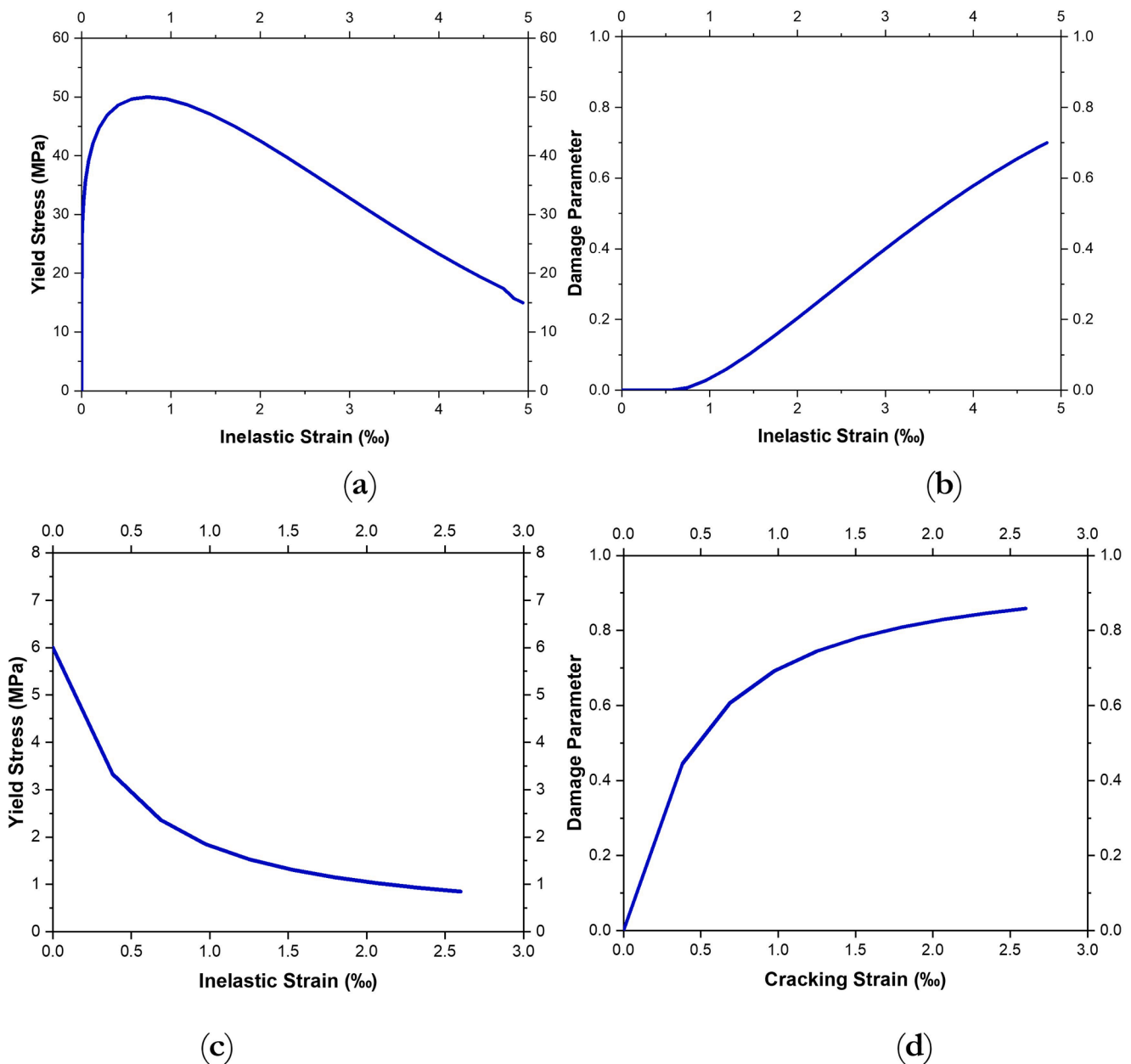


Fig. 18. Parameters of CDPM for input in ABAQUS of the experimental test of Nagy-György et al. (2012) [48]. (a) and (b) Compressive behavior concrete and compression damage; (c) and (d) Tensile behavior and concrete and tension damage.

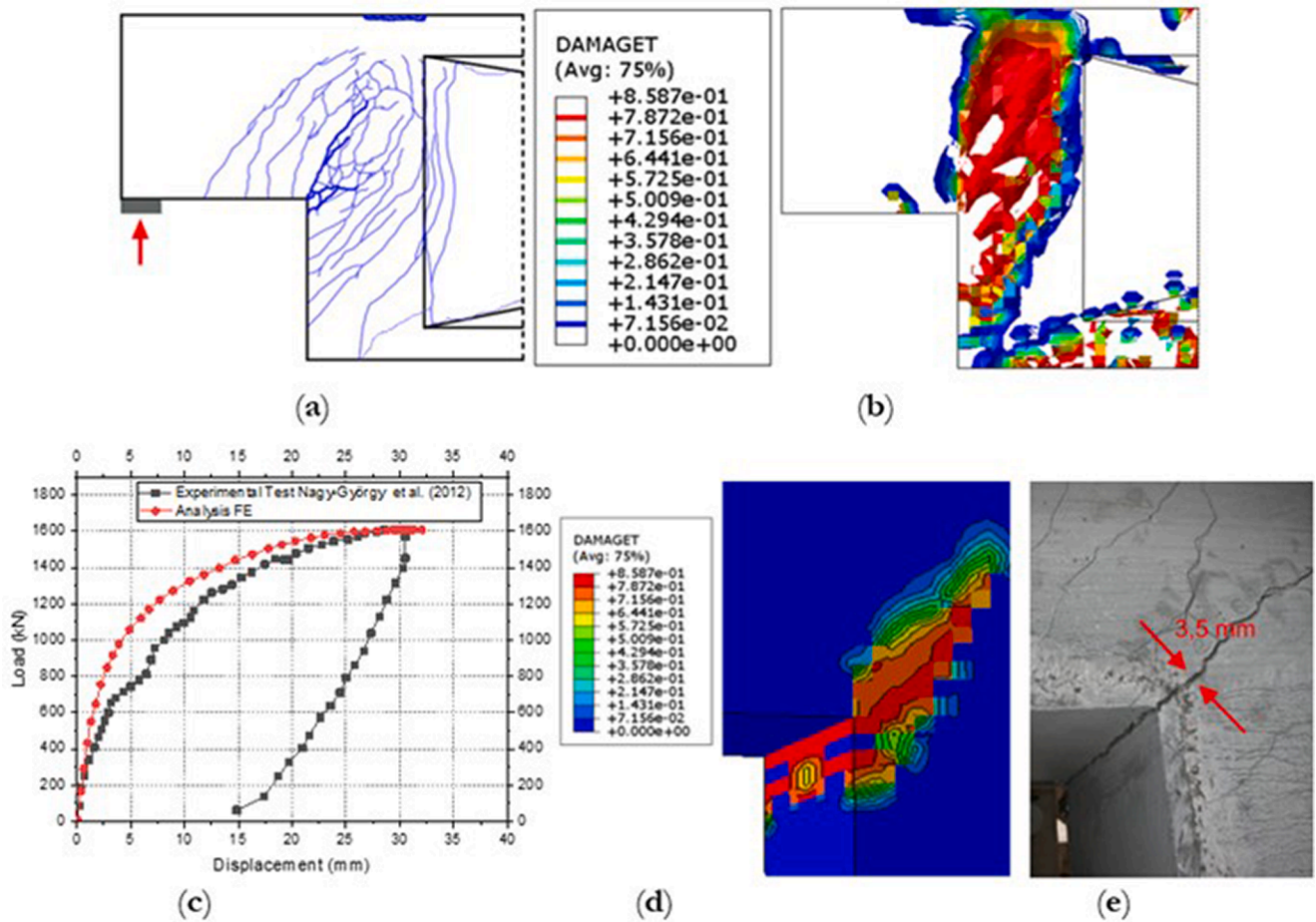


Fig. 19. Comparison of experimental results × numerical. (a) Crack map of the experimental test; (b) Crack surfaces obtained numerically (Damaged finite elements); (c) Experimental vs numerical result; (d) Tension damage path on finite elements in half-joint beam (e) Crack value in the half-joint beam of 3.50 mm [52].

[11]. Where the stress $\sigma_{c(1)}$ is the compression stress in phase 1; E_0 is the initial (undamaged) modulus of the material; and ϵ_c : strain in compression.

Already in phase 2: The second segment of the graphic is quadratic (see Fig. 16a), represents the hardening of the concrete and occurs between $0.4f_{cm}$ e f_{cm} i.e, is defined when the compressive stress is achieved $\sigma_c = 0.4f_{cm}$, cracks begin to appear accordingly, the relationship of stress–strain of concrete in this phase is nonlinear behavior. Phase 3: The behavior of concrete in this phase is softening and determined based on the theory which is proposed by Kratzig and Polling (2004) [54]. The ascending stretch is taken as linear-elastic and the descending one is designated based on the exponential expression derived from experimental tests Cornellissen et al. [55,56].

This model is suitable for numerical analysis because the model

depends on the length of mesh elements l_{eq} . Therefore, the third (descending) segment is obtained the maximum damage in concrete d_c . Regarding to concrete submitted to tension (Fig. 16b), the curve presents two segments. The first one is linear until the limit stress, while, the second one represents the softening of the material after microcracks opening [57].

The characteristic of this curve is that it does not depends on the element meshing in the FE model. Therefore, with the curves of strength of the concrete the compressive and tensile, it is possible to obtain the damage parameters, indicated by $\epsilon_c^{pl,h}$ and $\epsilon_t^{pl,h}$, which refers to equivalent plastic strains in compression and tension, respectively as follows [57].

$$\epsilon_c^{pl,h} = \epsilon_c^{in,h} - \frac{d_c}{(1 - d_c)} \frac{\sigma_c}{E_0} \tag{1}$$



Fig. 20. Extraction of specimens to determine compressive strength.

Table 4
Properties of steel reinforcement material.

Description of steel properties	Values used in numerical simulation
Diameter (mm)	12.50;16.0;20.0;25.0
Steel Density [tonne/mm ³]	7.85e-9
Yield Stress f_y [MPa]	441.50
Yield strain ϵ_y [%]	2.1×10^{-3}
Ultimate Strength f_{ult} [MPa]	622.11
Elastic modulus E_s [MPa]	201,150
Poisson's ratio ν	0.30

$$\epsilon_r^{pl,h} = \epsilon_r^{in,h} - \frac{d_t}{(1 - d_t)} \frac{\sigma_r}{E_0} \quad (2)$$

5.2. Validation of numerical simulation with ABAQUS

To validate the numerical results performed in this work with FE static analysis, using ABAQUS, it was initially simulated, a reinforced concrete dapped-end beams, also known as half-joints with a length of 20.0 m and a height of 1.50 m tested by Nagy-György et al. (2012) [48]. The material properties were determined from laboratory tests, in conformity with [58] for concrete and [59] for steel. A concrete with a maximum aggregate size of 16 mm and mean compressive cube strength of 56 N/mm² was used, corresponding to a C-50 concrete strength class. Characteristic values of the tensile properties of the steel reinforcements are presented in Table 3, while the concrete results using the CDPM in the numerical simulation are shown in Fig. 17 and Fig. 18, all materials according to work of Nagy-György et al. (2012) [48].

In ABAQUS it is possible to define different constitutive laws, from

the stress–strain relationship for steel reinforcing bars. In this paper, the bilinear constitutive law was adopted. The parameters defined by the modulus of elasticity and steel yield strength were used from Table 3, respectively.

The modeling results are shown in Fig. 19. The behavior of the half-joint beam tested by Nagy-György et al. (2012) [48] was used to compare with numerical simulation using concrete damage. The values of numerical load were compared with the experimental to calibrate the plasticity parameters, as shown in Table 2. The numerical model presented a failure mode similar to the experimental.

From of the plasticity parameters calibrated in this section ($K_c, \psi, f_{b0}/f_{c0}, \epsilon, \mu$), was used in the model of the bridge over the Pianco River was simulated, also considering concrete density of 2000 [kg/m³], for quasi-static dynamic analysis using Dynamic Explicit algorithm in ABAQUS, changing only the parameters of strength of the concrete, as a parametric study, as presented in the following section.

5.3. Input data for CDPM modeling in ABAQUS with boundary conditions of the bridge

In order to have a more realistic model, it was used the compressive strength of the concrete obtained experimentally by extraction of ten concrete specimens removed from the bridge beam near the abutment to determine the compressive strength, in which it was obtained the compressive strength of approximately 22 MPa and $E_c = 26,043$ MPa. The Fig. 20 shows the concrete extraction on the bridge, as well as the respective concrete compression test. While Table 4 presents the parameters of the steel used in the modeling of the bridge in ABAQUS through of extraction of small steel bars, of the abutment of the bridge called the CA-50.

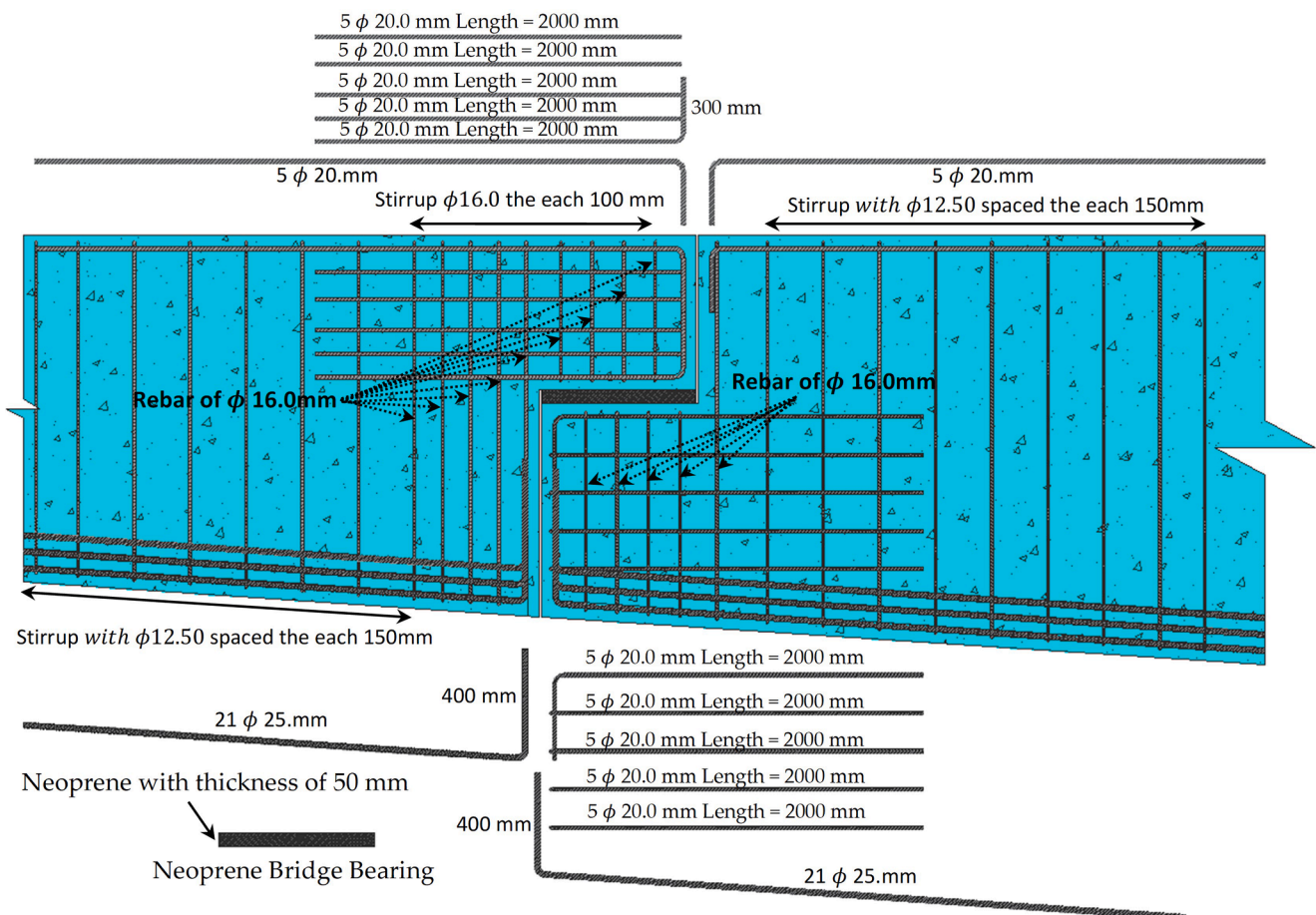


Fig. 21. Details of the bars of the Gerber of the bridge over the Pianco River.

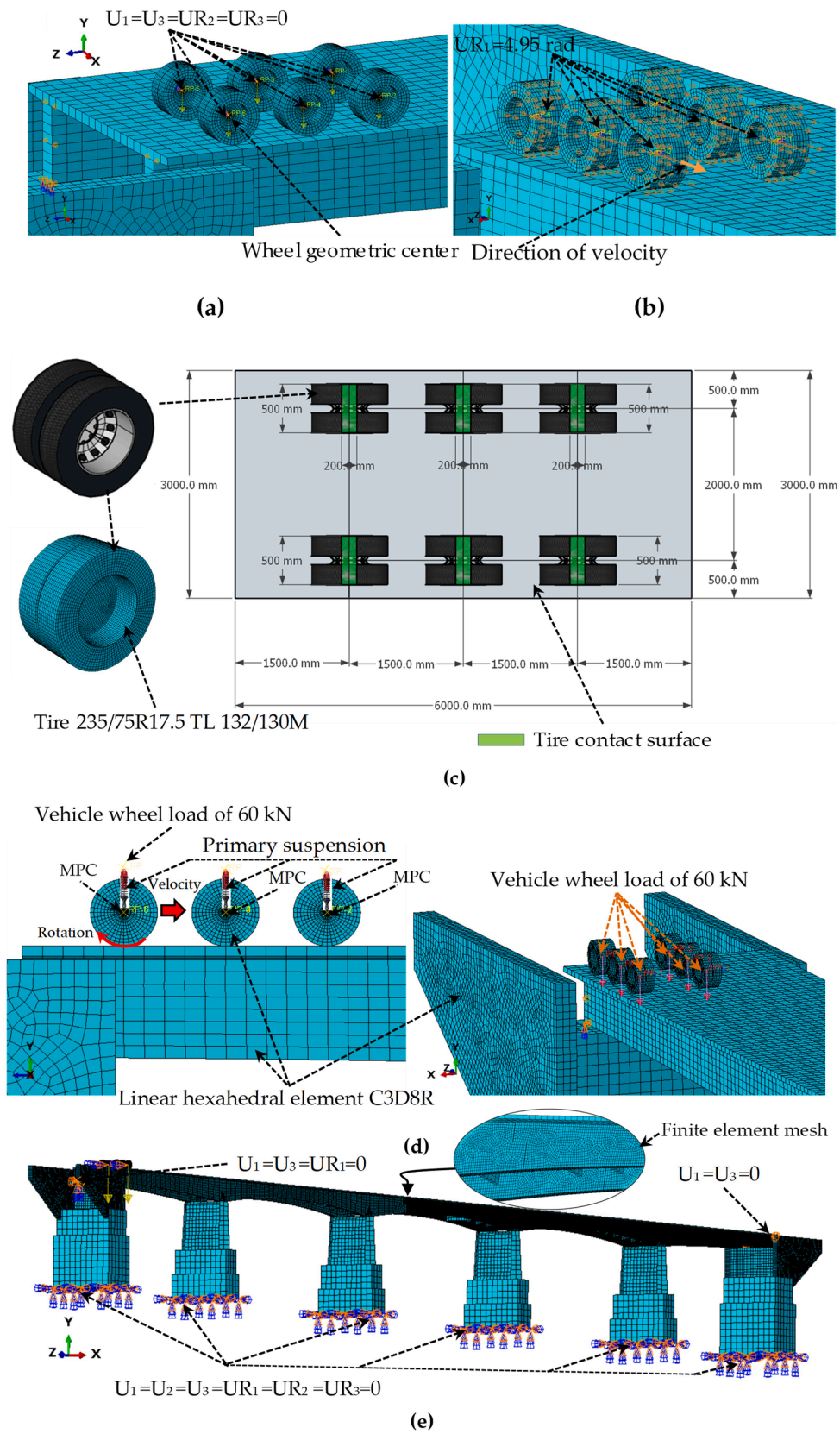


Fig. 22. Vehicle live loading TB-360 kN. (a) Vehicle tire setup; (b) Tangential velocity direction; (c) Plan view of vehicle tires; (d) Conditions for applying the point load; (e) 3D model.

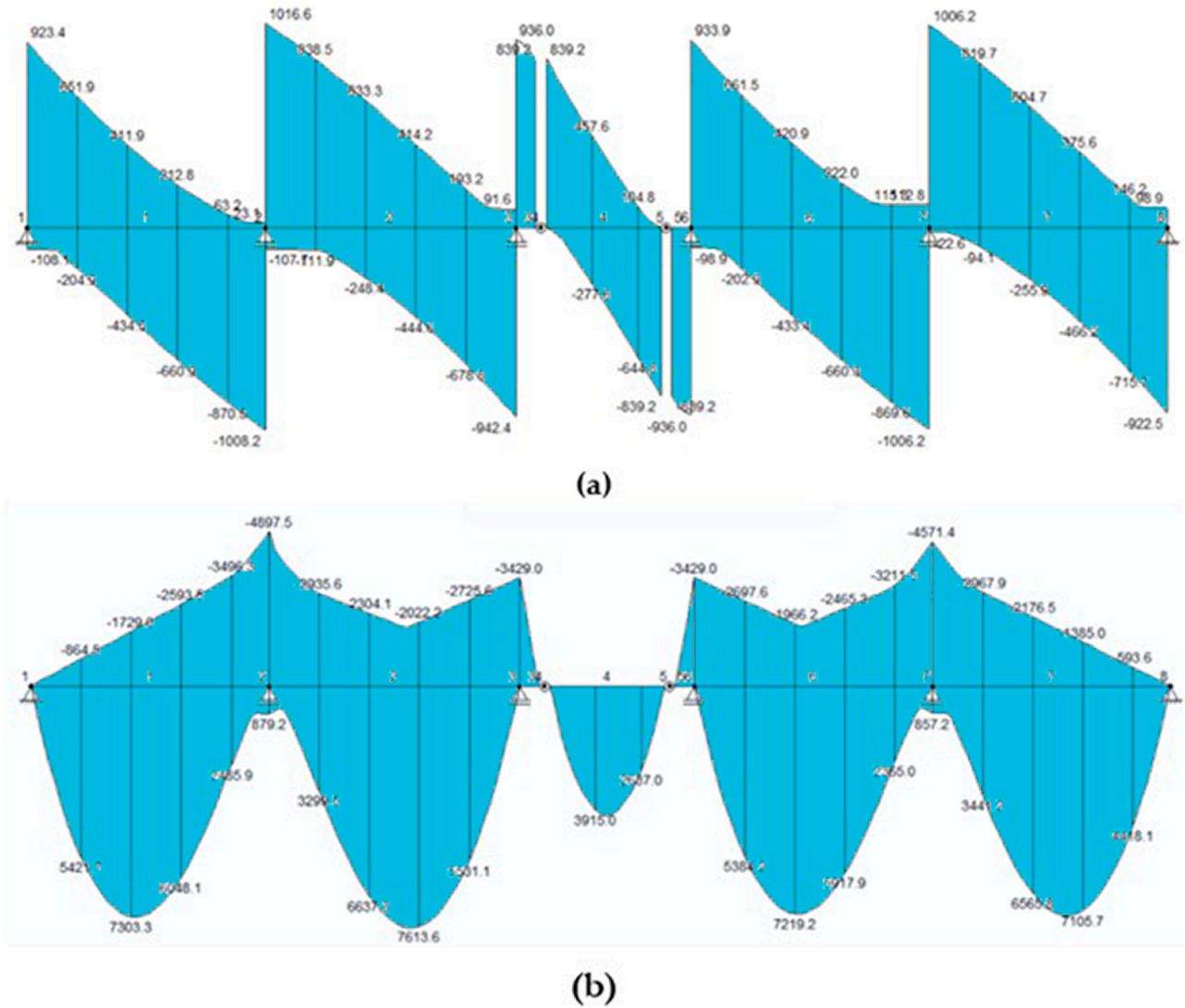


Fig. 23. Shear force and bending moment diagram in the girder of the Bridge. (a) Shear force diagram and (b) Bending moment diagram.

A 3D model of the bridge was numerically simulated using ABAQUS software, which considered the bars steel reinforcement in the girders of the bridge with typical support in Gerber (See Fig. 21). The beam has a variable parabolic section, close to the Gerber the section has a height of 185.00 cm with a width of 60.00 cm and a half-joint of 105.00 cm in the support. The connecting base between the two beams on the Gerber is 75.00 cm with a 50.00 mm neoprene plate. In detail, the girders of the bridge were simulated using solid element type C3D8R with 8 points of Gaussian with integration reduced.

The bars were modeled with T2D3 element which is only under tension and compression conditions. Interaction between bar and concrete using embedded algorithm. This method allows a node or group of nodes of bar to be constrained to the kinetic boundary conditions with the nodes in the concrete elements [52]. The interaction between the chartered neoprene plate and the concrete beam was used the contact with Coulomb friction with the friction coefficient equal to 0.6 [60]. On the other hand, the transmitted compressive stress between the contact surfaces was unlimited, between the surface of the tire of the load train and the bridge pavement. The tangential behavior was simulated by “Penalty Friction.” In the Classical Coulomb Friction Model, the critical friction stress depends on the contact pressure and the elastic slip was allowed on the contact surface [61]. Assuming that the friction coefficient μ_0 between the contact surfaces was the same 0.1 of the master and

slave surface [62]. The simulation model of the dynamic friction due to tire-pavement contact was created in a three-step process. Specifically, a 3D model was built, then the steady state of the kinetic contact was analyzed in ABAQUS/Standard solver based upon static contact [63]. Considering the steady-state rolling analysis of a tire of ABAQUS 6.10 Example Problem Manual [64], three steps were used to create the 3D models of grooving radial tires: (1) simplification before modeling, (2) importing a 2D tire cross-sectional model into ABAQUS, and (3) 3D model generation of pneumatic tire [60]. Details of the modeling with vehicle live loading in FE and also of the bridge are shown in Fig. 22.

Fig. 22 presents a specific MPC constraint created for the control point at the geometric center between the two wheels live loading vehicle to include the boundary conditions at the constraint point. To allow which the tire could move a condition was established, with UR1 = 4.95 rad, allowing rigid body rotation, while that a tangential velocity was assumed resulting in tire displacement over the bridge pavement. Due to the complexity of concrete with steel bars, the simulation was performed with ABAQUS/Explicit.

5.4. Results of static simulations

The analysis of Dapped-end beam is very complex and there is no unified theory that is universally accepted [65]. First, a numerical

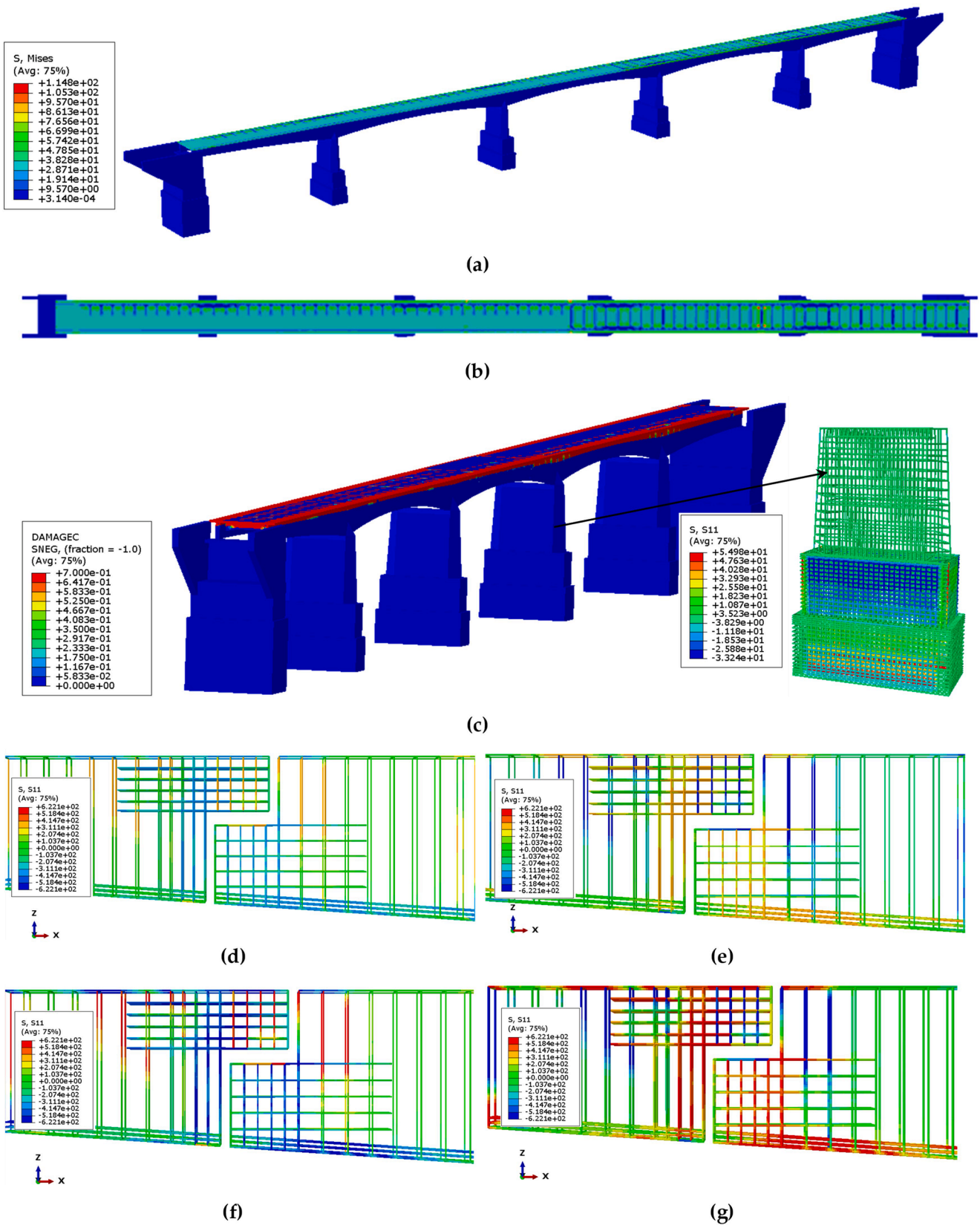


Fig. 24. Static results of the bridge with CPDM in ABAQUS. (a) Von Mises stresses in bridge concrete; (b) Stresses in the bridge slab pavement; (c) Stresses in the concrete and steel of the bridge column; (d) to (g) Dapped-end beam of the bridge with 25%, 50%, 75% and 100% of ultimate-strength on the bars of steel, respectively; (h) to (k) Dapped-end beam of the bridge with 25%, 50%, 75% and 100% of ultimate-strength of concrete with damage in crush; (l) and (m) Dapped-end beam of the bridge with 50% and 100% of ultimate-strength of concrete in tension with tension damage equal to 0.93. (n) Support type neoprene bridge bearing pads; (o) to (q) stress in bridge elastomeric bearings.

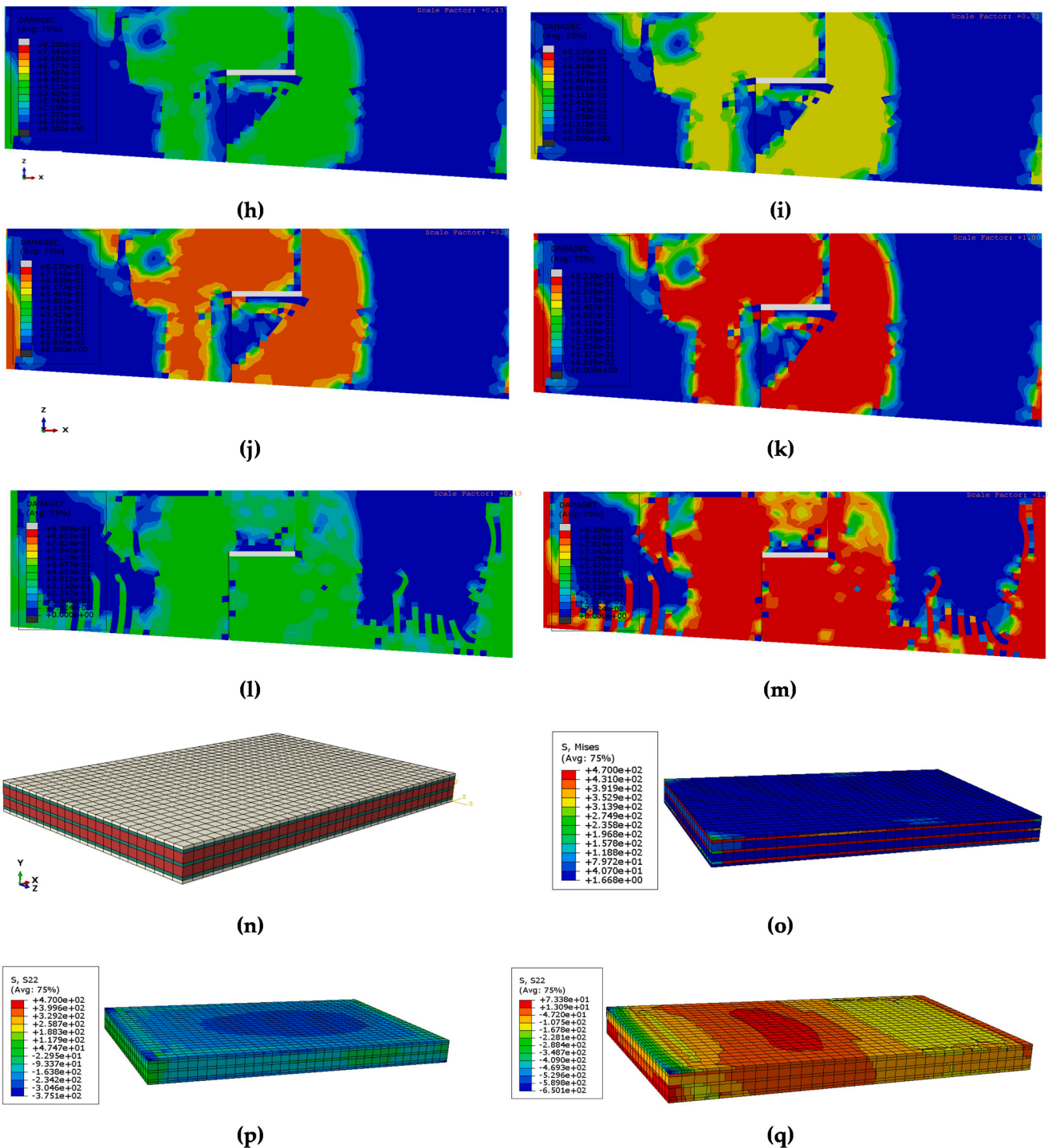


Fig. 24. (continued).

simulation of the bridge with linear element was carried out with the FTOOL software using the normative vehicle TB-360 [66] that considers the original conditions of the bridge when it was designed, later, the shear forces and also the envelope of bending moment were evaluated, the Fig. 23 shows the results. On the other hand, a non-linear FE model was carried out to evaluate the mechanical behavior of the bridge's Gerber shown in Fig. 21. The results due to vehicle live loading TB-360 kN [66] on the bridge's Gerber are shown in Fig. 24.

In addition to evaluate the stresses in the concrete and steel of the bridge, the support of the bridge was also evaluated using elements type C3D8RH, that are available in the ABAQUS/Standard library (C3D8RH:

8-node linear brick). FE model in the three-dimensional space consisted of 140,124 finite elements. With data from the constitutive model of Gajewski et al. [67].

The designed structure has strenght within the parameters of the ultimate limit state for the safety of the structure and its users by limiting the stress that materials experience. In order to comply with engineering demands for strength and stability under design loads (vehicle live loading TB-360 kN [66]). The Fig. 25 shows the ultimate strength of the Gerber of the bridge obtained in the numerical simulation with nonlinear FE. While the ultimate limit state of the beam is also shown in the plot with shear envelope force of 936 kN.

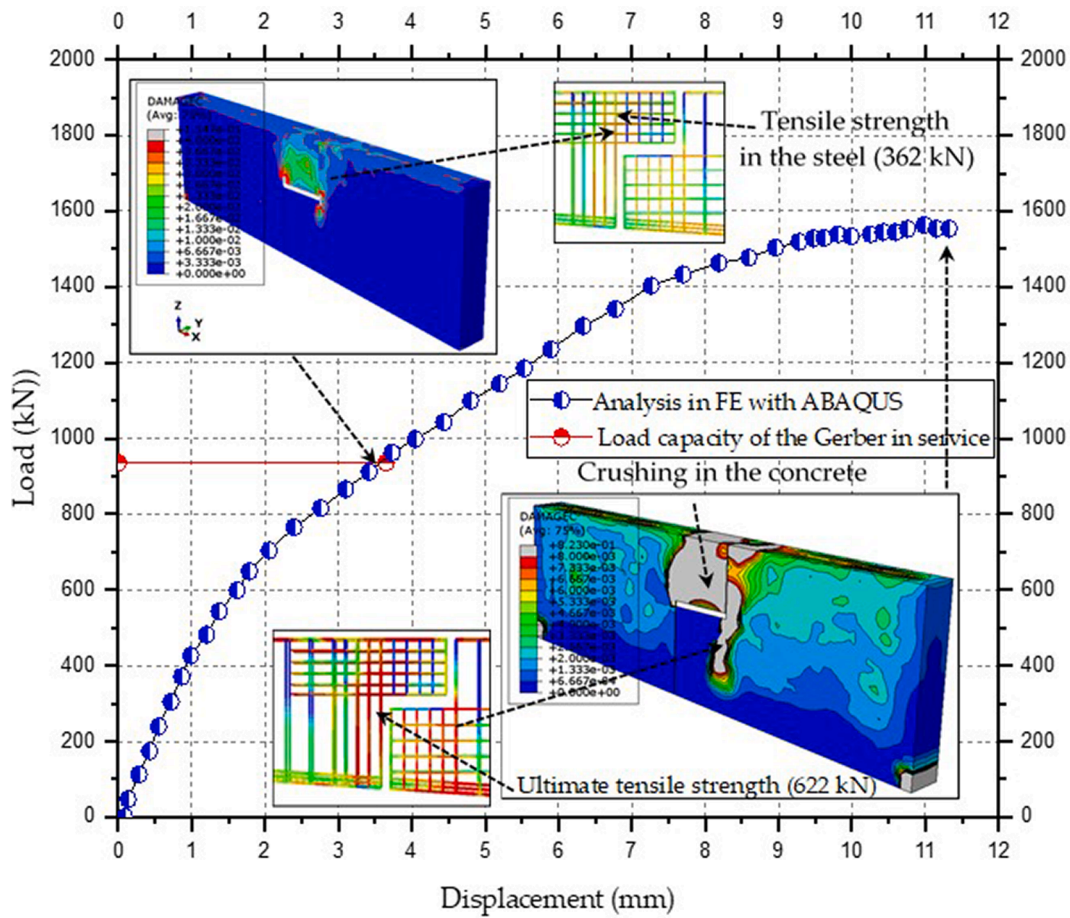


Fig. 25. Load carrying capacity of the Gerber from the bridge over the Pianco river.

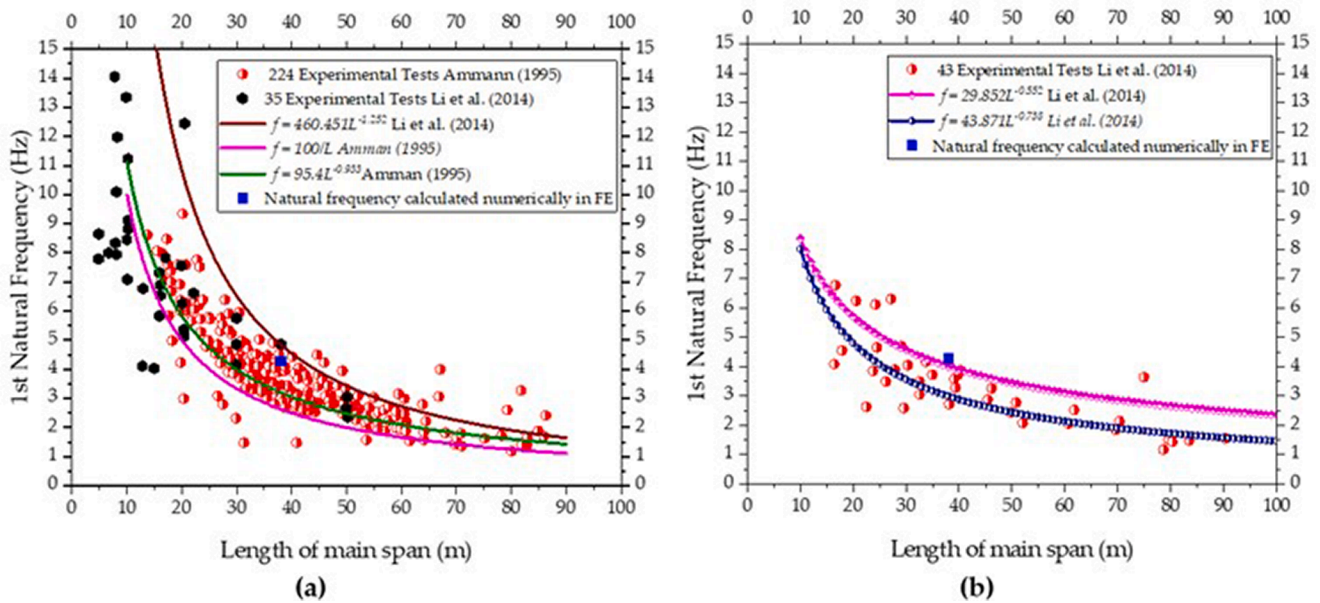


Fig. 26. Comparison of the numerical result in comparison to experimental values for simply supported and continuous bridges. (a) Fundamental frequency for bridges with supported spans and (b) Comparison of the result for fundamental frequency in relation to bridges with continuous spans.

Table 5
Relationship between first-mode natural frequencies and length of main spans.

Types of span of the Bridge	Authors of technical literature	Length of main span (m)	Equation for natural frequency	1st Natural Frequency (Hz)	Correlation Coefficient R ²	Values obtained in ABAQUS (Hz)
Simply supported	Ammann (1995) [77]	38.0	$f = 100/L$	2.63	0.8799	4.26
	Ammann (1995) [77]	38.0	$f = 95.4L^{-0.933}$	3.20	0.5821	
	Li et al. (2014) [76]	38.0	$f = 460.451L^{-1.252}$	4.85	0.9097	
Continuous rigid-frame	Li et al. (2014) [76]	38.0	$f = 29.8521L^{-0.552}$	4.01	0.5627	
Continuous	Li et al. (2014) [76]	38.0	$f = 43.871L^{-0.738}$	2.99	0.6843	

5.5. Dynamic evaluation of the bridge over the Pianco River

Natural frequencies are useful information for bridges, as they relate closely to the stiffness of the bridge [68]. In some applications, the bridge frequencies, especially of the fundamental mode, have been used as an index of structural integrity or health condition [69–74], because it is a non-destructive method of structural evaluation [75]. In this paper, the bridge structure was modeled with CDPM through ABAQUS using the geometry obtained from the TLS. The mode shapes and the natural frequencies were obtained. The algorithm used in this analysis was the Linear Perturbation of the library in ABAQUS with number of eigenvalue equal to 6. The simulation result is shown in Fig. 26. The natural frequency result was applied for two types of structures, one with continuous beams and the other with simply supported beams. In this context, the values of natural frequencies were compared with the experimental results of Li et al. [76] and Amman (1995) [77].

The structural energy dissipation depends on many factors, such as the plastic development, damage, damping actions and so on [78–80]. Otherwise, for an elastic system, damping is the most important action which will induce vibration attenuation. For elastic–plastic analysis, plastic development and damage usually are the major inducements of energy dissipation [81]. Consequently, the damping ratios of the bridges decrease and tend toward stable values after a certain number of years, provided that, there is no damage increase in the structure, and maintenance be carried out for preserve the integrity of the structure [69]. Therefore, the forms of damage, the locations of damage, and the strengthening methods have a great influence on the changing of damping ratios, and consequently in the natural frequency of the structure [69]. Therefore, due to the complexity of obtaining the damping, the Rayleigh damping was used through the ABAQUS library, and compared with the experimental results of Li et al. [76]. For bridges with a structural system composed of beams with Gerber connection the fundamental frequency, more if approaches of bridges constituted up of isostatic spans.

The relationship of the first natural frequency is compared with different types of bridges shown in Table 5, where the frequency obtained in the technical literature was evaluated and compared with the results of the numerical simulation with ABAQUS, for the bridge over the Pianco River with a free span of 38.00 m. Therefore, the results of natural frequencies compared with bridges with continuous spans, did not present a good correlation, according to the values found by Ulker-Kaustell and Karoumi (2011) [80], Idris et al. (2016) [82] and also for Li et al. (2014) [76], while the results compared to bridges with supported spans showed better results and are in agreement with Bachmann and Ammann (1987) [83], Ammann (1995) [77], Li et al. (2014) [76] and Lin and Yang (2005) [84].

The Fig. 27 shows the six bridge mode shapes; the first mode shape is a flexural mode. The second and third mode shapes reflects the vibration of the two girders of the midspan of the bridge. On the other hand, in the fourth mode shape and also in the fifth mode shapes the structure

showed behavior of the longitudinal beams and beams transverses with distortion in the Gerber's type supports. Finally, the sixth mode shape, the structure behavior was mainly defined by bending and torsional vibration of the two longitudinal girders and also transverses beams in the midspan of the bridge.

6. Conclusions

Over the past few decades, remote sensing techniques have been used increasingly in structural engineering. This paper introduced an evaluation system for reverse engineering using a 3D laser scanner of the Trimble. Bridge designers are using the terrestrial laser scanning tool to assist in the elaboration of the digital model of the bridge elements. Thus, the aim of the present study was to demonstrate the capacity of the use of TLS in obtaining the existing geometry of the bridge to provide a detailed information to carry out a numerical simulation of the digital model of the bridge with nonlinear analysis in FE. Photogrammetry was also applied in the As-built survey of the bridge and integrated with the TLS point cloud to create the bridge's digital model. A damage plasticity model was then applied to the digital model of the bridge to perform a static and dynamic analysis. Therefore, the main conclusions of the work are presented as follows:

- (1) Using TLS with point scanning was able to generate a digital model of the bridge successfully. Moreover, with georeferenced scanning it was easier to identify all the scenes captured with the Trimble Access application during field survey. On the other hand, the creation of the 3D model of the bridge in REVIT was facilitated using the Trimble SketchUp tool, which all the parameterization of the bridge was created in the BrIM criteria implemented in PROARTE.
- (2) The technical literature only shows the use of TLS without the photogrammetry to perform AsBuilt in the generation of the digital model. Therefore, the main contribution of this paper was show that from the digital model of the bridge it is possible to carry out a structural analysis of the behavior of the bridge with ABAQUS.
- (3) Therefore, the live load of the standard vehicle denominated of TB-360 kN based on the standard NBR 7188 (1982) [85], applied in the bridge analysis showed satisfactory strength for the load train. In which the strength of the Gerber was of 66.67% over the ultimate strength of the structural element. However, it was observed in the numerical simulation that the steel plates of the elastomeric bearing have stresses next to the ultimate strength of the steel plate (470 MPa), with values above the recommended by manufacturers in Brazil. For this reason, the PROARTE adopted a solution for the rehabilitation of the bridge, making the total joint of the two girders with of the Gerber-type support, removing of the elastomeric bearing type support devices.

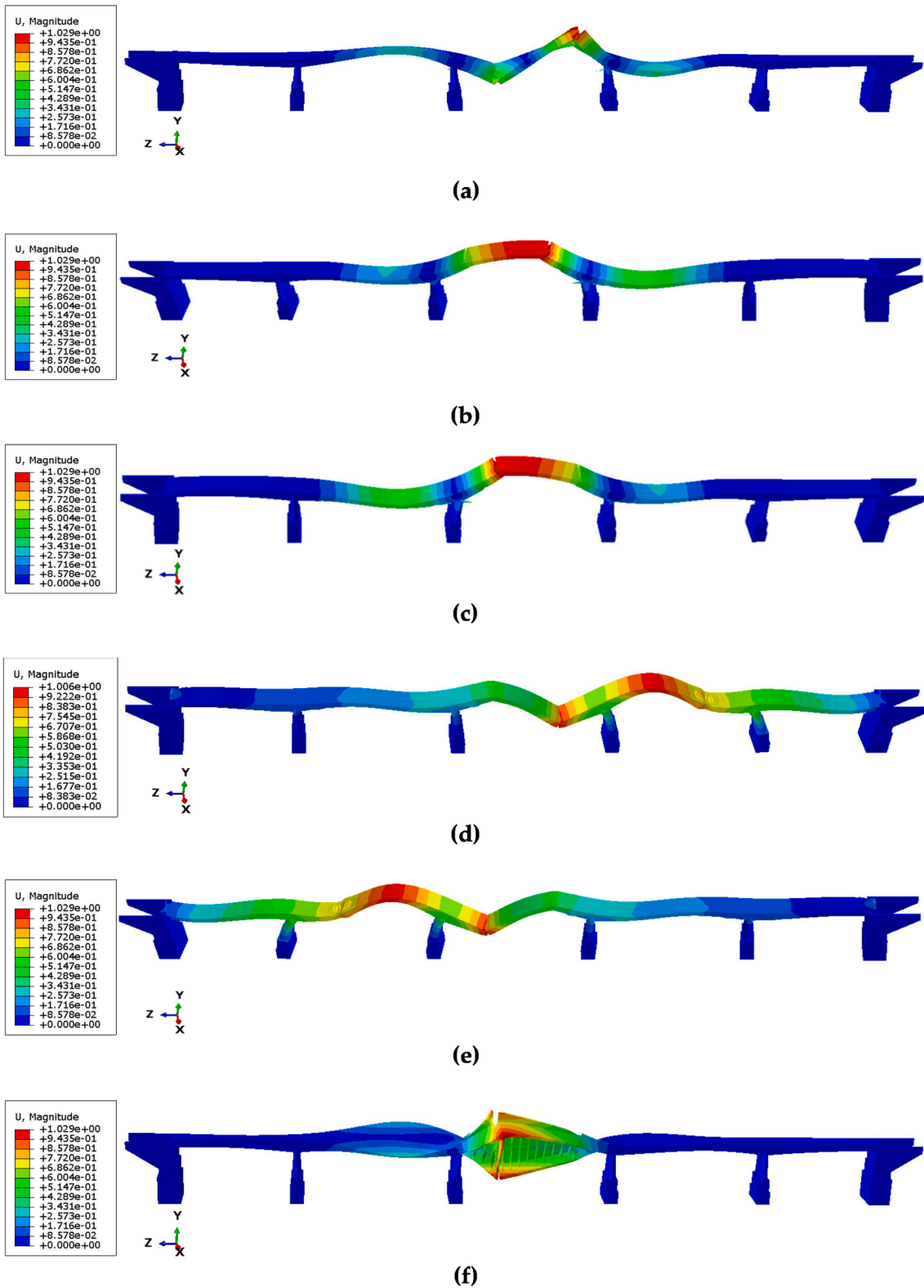


Fig. 27. Bridge mode shapes; (a) First mode shape ($f_1 = 4.26$ Hz); (b) Second mode shape ($f_2 = 6.27$ Hz); (c) Third mode shape ($f_3 = 12.31$ Hz); (d) Fourth mode shape ($f_4 = 19.05$ Hz); (e) Fifth mode shape ($f_5 = 24.18$ Hz); (f) Sixth mode shape ($f_6 = 27.81$ Hz).

- (4) The dynamic analysis presented results compatible with the technical literature considering the first natural frequency equal the 4.26 Hz.
- (5) The average values of the damping ratio of the structure for simply supported bridges presented values around 2.28 % with a standard deviation of 0.87 %, which present a good correlation with the numerically found values. Furthermore, the value obtained in the numerical simulation with ABAQUS, for the damping ratio was 2.4 %, which is within the range of the experimental values found in the technical literature.

Funding

This research received no external funding.

CRediT authorship contribution statement

Wellington Vital: Software, Validation, Formal analysis, Investigation, Resources, Data curation, Writing – original draft, Writing – review & editing, Visualization, Supervision, Project administration, Funding acquisition. **Ramon Silva:** Software, Validation, Formal analysis, Investigation, Resources, Data curation, Writing – original draft, Writing – review & editing, Visualization, Supervision, Project administration, Funding acquisition. **Marcus V.G. de Moraes:** Software, Validation, Formal analysis, Investigation, Resources, Data curation, Writing – original draft, Writing – review & editing, Visualization, Supervision, Project administration, Funding acquisition. **Bruno Emidio Sobrinho:** Software, Validation, Formal analysis, Investigation, Resources, Data curation, Writing – original draft, Writing – review & editing, Visualization, Supervision, Project administration, Funding acquisition. **Rodrigo Pereira:** Software, Validation, Formal analysis, Investigation, Resources, Data curation, Writing – original draft, Writing – review & editing, Visualization, Supervision, Project administration, Funding acquisition. **Francisco Evangelista:** Software, Validation, Formal analysis, Investigation, Resources, Data curation, Writing – original draft, Writing – review & editing, Visualization, Supervision, Project administration, Funding acquisition.

Declaration of Competing Interest

The authors declare that they have no known competing financial interests or personal relationships that could have appeared to influence the work reported in this paper.

Acknowledgement

The authors wish to thank DNIT(Brazilian National Department of Transport Infrastructure), Engemap Group Engineering, TOMASINI Topographic Equipment and Exact Engineering. The authors are also thankful to the Research Support Foundation(FAP-DF) and Graduation Program in Structural Engineering of the University of Brasilia.

References

- [1] P.d.T.C. Mendes, Contribution to a concrete bridge management model applied to the Brazilian highway network, Ph.D. Thesis, University of São Paulo, São Paulo, Brazil, 2009. Accessed on 04/25/2022.
- [2] A.F. Santos, M.S. Bonatte, H.S. Sousa, T.N. Bittencourt, J.C. Matos, Improvement of the inspection interval of highway bridges through predictive models of deterioration, *Buildings* 12 (2022) 124, <https://doi.org/10.3390/buildings12020124>.
- [3] F. Potenza, C. Rinaldi, E. Ottaviano, V. Gattulli, A robotics and computer-aided procedure for defect evaluation in bridge inspection, *J. Civil. Struct. Health Monit.* 10 (3) (2020) 471–484, <https://doi.org/10.1007/s13349-020-00395-3>.
- [4] A. Girardet, C. Botton, A parametric BIM approach to foster bridge project design and analysis, *Autom. Constr.* 126 (2021) 103679, <https://doi.org/10.1016/j.autcon.2021.103679>.
- [5] M. Rashidi, M. Mohammadi, S. Sadeghlou Kivi, M.M. Abdolvand, L. Truong-Hong, B. Samali, A decade of modern bridge monitoring using terrestrial laser scanning: review and future directions, *Remote Sens.* 12 (2020) 3796, <https://doi.org/10.3390/rs12223796>.
- [6] F. Tang, T. Ma, J. Zhang, Y. Guan, L. Chen, Integrating three-dimensional road design and pavement structure analysis based on BIM, *Autom. Constr.* 113 (2020), 103152, <https://doi.org/10.1016/j.autcon.2020.103152>.
- [7] Alexa Mitchell, Implementing 3-D and 4-D modeling software to enhance bridge design: Research Spotlight. Departamento de Transportes de Michig, Report Number: SPR-1647, 2018, <https://rosap.nrl.bts.gov/view/dot/36541>.
- [8] G. Tzortzinis, C. Ai, S. Gerasimidis, Using 3D laser scanning for estimating the capacity of corroded steel bridge girders: Experiments, computations and analytical solutions, *Eng. Struct.* 265 (2022) 0141–0296, <https://doi.org/10.1016/j.engstruct.2022.114407>.
- [9] R. Xiao, Y. Lian, B. Sun, X. Zhao, Z. Liu, P. Tang, Method of bridge structural analysis based on bridge information modeling, *Comput. Civil Eng.* 10 (2017) 012.
- [10] O.G. Sánchez-Rivera, P.-Díaz H. Galvis-Guerra, Y.D. Ardila-Chacón, C.A. Martínez-Martínez, Br IM 5D models and Lean Construction for planning work activities in reinforced concrete bridges, *Rev. Fac. Ing.* 26 (46) (2017) 39–50. <https://doi.org/10.19053/01211129.v26.n46.2017.7314>.
- [11] J. Woetzel, N. Garemo, J. Mischke, P. Kamra, R. Palter, *Bridging Infrastructure Gaps: Has the World Made Progress*, McKinsey & Company, New York, NY, USA, 2017.
- [12] S. Kaewunruen, J. Sresakoolchai, Z. Zhou, Sustainability-based lifecycle management for bridge infrastructure using 6D BIM, *Sustainability* 12 (2020) 2436, <https://doi.org/10.3390/su12062436>.
- [13] S.S. Chen, A.M. Shirole, Integration of information and automation technologies in bridge engineering and management, *Transport. Res. Record: J. Transport. Res. Board* 1976 (1) (2006) 2–12. <https://doi.org/10.1177/0361198106197600101>.
- [14] R. Sacks, Evaluation of economic impact of three-dimensional modeling in precast concrete engineering, *J. Comput. Civ. Eng.* 18 (4) (2004) 301–312, [https://doi.org/10.1061/\(ASCE\)0887-3801\(2004\)18:4\(301\)](https://doi.org/10.1061/(ASCE)0887-3801(2004)18:4(301)).
- [15] N.-S. Dang, G.-T. Rho, C.-S. Shim, A master digital model for suspension bridges, *Appl. Sci.* 10 (2020) 7666, <https://doi.org/10.3390/app10217666>.
- [16] ABNT NBR 9452, Inspection of Concrete Bridges and Footbridges—Procedures. Associação Brasileira de Normas Técnicas, Rio de Janeiro, Brazil, 2019.
- [17] DNIT 010; Inspeções em pontes e viadutos de concreto armado e protendido—Procedimento, Departamento Nacional de Infraestrutura de Transportes, Rio de Janeiro, Brazil, 2004.
- [18] ABNT NBR 7188, Road and Pedestrian Live Load on Bridges, Viaducts, Footbridges and Other Structures, Associação Brasileira de Normas Técnicas, Rio de Janeiro, Brazil, 2013.
- [19] R. Jiang, D.V. Jáuregui, K.R. White, Close-range photogrammetry applications in bridge measurement: Literature review, *Measurement* 41 (8) (2008) 823–834, <https://doi.org/10.1016/j.measurement.2007.12.005>.
- [20] C. Koch, S. German Paal, A. Rashidi, Z. Zhu, M. König, I. Brilakis, Achievements and challenges in machine vision-based inspection of large concrete structures, *Adv. Struct. Eng.* 17 (3) (2014), <https://doi.org/10.1260/1369-4332.17.3.30>.
- [21] B. McGuire, R. Atadero, C. Clevenger, M. Ozbek, Bridge information modeling for inspection and evaluation, *J. Bridge. Eng.* 21 (4) (2016), [https://doi.org/10.1061/\(ASCE\)BE.1943-5592.0000850](https://doi.org/10.1061/(ASCE)BE.1943-5592.0000850).
- [22] B. Riveiro, M.J. DeJong, B. Conde, Automated processing of large point clouds for structural health monitoring of masonry arch bridge, *Autom. Constr.* 72 (2016) 258–268, <https://doi.org/10.1016/j.autcon.2016.02.009>.
- [23] M. Sedek, A. Serwa, Development of new system for detection of bridges construction defects using terrestrial laser remote sensing technology. National authority for remote sensing and space sciences, *Egyptian J. Rem. Sens. Space Sci.* (2015), <https://doi.org/10.1016/j.ejrs.2015.12.005>.
- [24] A. Bono, L. D'Alfonso, G. Fedele, A. Filice, E. Natalizio, Path planning and control of a UAV fleet in bridge management systems, *Remote Sens.* 2022 (1858) 14, <https://doi.org/10.3390/rs14081858>.
- [25] G. Santarsiero, A. Masi, V. Picciano, A. Digrisolo, The Italian guidelines on risk classification and management of bridges: Applications and remarks on large scale risk assessments, *Infrastructures* 6 (2021) 111, <https://doi.org/10.3390/infrastructures6080111>.
- [26] E. Lachat, T. Landes, P. Grussenmeyer, Investigation of a combined surveying and scanning device: The trimble SX10 scanning total station, *Sensors* 17 (2017) 730, <https://doi.org/10.3390/s17040730>.
- [27] A. Jang, Y.K. Ju, M.J. Park, Structural stability evaluation of existing buildings by reverse engineering with 3D laser scanner, *Remote Sens.* 14 (2022) 2325, <https://doi.org/10.3390/rs14102325>.
- [28] D.V. Jáuregui, Y. Tian, R. Jiang, Photogrammetry applications in routine bridge inspection and historic bridge documentation, *Transp. Res. Rec.: J. of the T. R. B.* 1958 (1) (2006) 24–32. <https://doi.org/10.1177/0361198106195800103>.
- [29] S.I. Deliry, U. Avdan, Accuracy of unmanned aerial systems photogrammetry and structure from motion in surveying and mapping: A, *Sens* 49 (8) (2021) 1997–2017, <https://doi.org/10.1007/s12524-021-01366-x>.
- [30] H.T. Abdelwahab, Intelligent design (4D, 5D and beyond) for road design and construction projects: Two case studies, in: *International Road Federation (IRF) Examiner*, 12, 2017, pp. 21–25 <https://www.irf.global/ebooks/IRF-Examiner-17-Vol12.pdf>.
- [31] E. Lachat, T. Landes, P. Grussenmeyer, First experiences with the Trimble SX10 scanning total station for building facade survey, *Int. Arch. Photogramm. Remote Sens. Spatial Inf. Sci.* XLII-2/W3 (2017) 405–412, <https://doi.org/10.5194/isprs-archives-XLII-2-W3-405-2017>.
- [32] H. Son, F. Bosché, C. Kim, As-built data acquisition and its use in production monitoring and automated layout of civil infrastructure: A survey, *Adv. Eng. Inf.* 29 (2) (2015) 172–183, <https://doi.org/10.1016/j.aei.2015.01.009>.

- [33] G. Santarsiero, A. Masi, V. Picciano, Durability of gerber saddles in RC bridges: Analyses and Applications (Musmecc Bridge, Italy), *Infrastructures* 6 (2021) 25, <https://doi.org/10.3390/infrastructures6020025>.
- [34] C. Li, H. Hao, K. Bi, Numerical Study on the Seismic Performance of Precast Segmental Concrete Columns under Cyclic Loading, *Eng. Struct.* 148 (2017) 373–386, <https://doi.org/10.1016/j.engstruct.2017.06.062>.
- [35] J. Lubliner, J. Oliver, S. Oller, E. Onate, A plastic-damage model for concrete, *Int. J. Solids Struct.* 25 (1989) 299–326, [https://doi.org/10.1016/0020-7683\(89\)90050-4](https://doi.org/10.1016/0020-7683(89)90050-4).
- [36] B. Alfarah, F. López-Almansa, S. Oller, New methodology for calculating damage variables evolution in plastic damage model for RC structures, *Eng. Struct.* 132 (January 2017) 70–86, <https://doi.org/10.1016/j.engstruct.2016.11.022>.
- [37] R. Silva, W.V. Silva, J.Y.d. Farias, M.A.A. Santos, L.O. Neiva, Experimental and numerical analyses of the failure of prestressed concrete railway sleepers, *Materials* 13 (7) (2020) 1704, <https://doi.org/10.3390/ma13071704>.
- [38] H. Othman, H. Marzouk, Applicability of damage plasticity constitutive model for ultra-high performance fibre-reinforced concrete under impact loads, *Int. J. Impact Eng.* 114 (2018) 20–31, <https://doi.org/10.1016/j.ijimpeng.2017.12.013>.
- [39] ABAQUS. User's Manual; Version 6.14-1, Dassault Systèmes Simulia Corp: Providence, RI, USA, 2014.
- [40] J. Ungermann, V. Adam, M. Classen, Fictitious rough crack model (FRCM): A smeared crack modelling approach to account for aggregate interlock and mixed mode fracture of plain concrete, *Materials* 13 (2020) 2774, <https://doi.org/10.3390/ma13122774>.
- [41] C. Li, H. Hao, K. Bi, Numerical study on the seismic performance of precast segmental concrete columns under cyclic loading, *Eng. Struct.* 148 (2017) 373–386, <https://doi.org/10.1016/j.engstruct.2017.06.062>.
- [42] F. Aslani, R. Jowkarmeimandi, Stress–Strain model for concrete under cyclic loading, *Mag. Concr. Res.* 64 (8) (2012) 673–685.
- [43] J. Lee, G.L. Fenves, Plastic-damage model for cyclic loading of concrete structures, *J. Eng. Mech.* 124 (1998) 892–900, [https://doi.org/10.1061/\(ASCE\)0733-9399\(1998\)124:8\(892\)](https://doi.org/10.1061/(ASCE)0733-9399(1998)124:8(892)).
- [44] S.M. Farnam, F. Rezaei, Simulation of crack propagation in prestressed concrete sleepers by fracture mechanics, *Eng. Fail. Anal.* 96 (2019) 109–117, <https://doi.org/10.1016/j.engfailanal.2018.09.012>.
- [45] W. Ren, L.H. Sneed, Y. Yang, R. He, Numerical simulation of prestressed precast concrete bridge deck panels using damage plasticity model, *Int. J. Concr. Struct. Mater.* 9 (1) (2015) 45–54, <https://doi.org/10.1007/s40069-014-0091-2>.
- [46] L.M. Silva, e, André L. Christoforo, R.C. Carvalho, Calibration of Concrete Damaged Plasticity Model parameters for shear walls, *Matéria (Rio de Janeiro)* 26 (1) (2021), <https://doi.org/10.1590/S1517-707620210001.1244>.
- [47] H. Dawood, M. ElGawady, J. Hewes, Behavior of segmental precast posttensioned bridge piers under lateral loads, *J. Bridg. Eng.* 17 (5) (2012) 735–746, [https://doi.org/10.1061/\(ASCE\)BE.1943-5592.0000252](https://doi.org/10.1061/(ASCE)BE.1943-5592.0000252).
- [48] T. Nagy-György, G. Sas, A.C. Dăescu, J.A.O. Barros, V. Stoian, Experimental and numerical assessment of the effectiveness of FRP-based strengthening configurations for dapped-end RC beams, *Eng. Struct.* 44 (2012) 291–303, <https://doi.org/10.1016/j.engstruct.2012.06.006>.
- [49] J. Lubliner, J. Oliver, S. Oller, E. Onate, A plastic-damage model for concrete, *Int. J. Solids Struct.* 25 (1989) 299–326, [https://doi.org/10.1016/0020-7683\(89\)90050-4](https://doi.org/10.1016/0020-7683(89)90050-4).
- [50] S. Oller, E. Onate, J. Oliver, J. Lubliner, Finite element nonlinear analysis of concrete structures using a -plastic-damage model, *Eng. F. Mech. Elsevier* 35 (1–3) (1990) 219–231, [https://doi.org/10.1016/0013-7944\(90\)90200-Z](https://doi.org/10.1016/0013-7944(90)90200-Z).
- [51] C. Le Thanh, H.-L. Minh, T. Sang-To, A nonlinear concrete damaged plasticity model for simulation reinforced concrete structures using ABAQUS, *Frattura ed Integrità Strutturale* 16 (59) (2021) 232–242, <https://doi.org/10.3221/IGF-ESIS.59.17>.
- [52] EC 2. Eurocode 2: Design of concrete structures, June 1992.
- [53] CEB-FIP, CEB-FIP Model Code 2010, London, LDN, UK, Thomas Telford, 2010. J. Fish, T. Belytschko, 2007, A first course in finite elements. John Wiley.
- [54] W.B. Krätzig, R. Pölling, An elasto-plastic damage model for reinforced concrete with minimum number of material parameters, *Comput. Struct.* 82 (15–16) (2004) 1201–1215, <https://doi.org/10.1016/j.compstruc.2004.03.002>.
- [55] H. Cornelissen, D. Hordijk, H. Reinhardt, Experimental determination of crack softening characteristics of normal weight and lightweight concrete, *Heron* 31 (2) (1986) 45–56.
- [56] J.G. Rots, R. De Borst, Analysis of concrete fracture in “direct” tension, *Int. J. Solids Struct.* 25 (12) (1989) 1381–1394, [https://doi.org/10.1016/0020-7683\(89\)90107-8](https://doi.org/10.1016/0020-7683(89)90107-8).
- [57] B. Alfarah, F. López-Almansa, S. Oller, New methodology for calculating damage variables evolution in Plastic Damage Model for RC structures, *Eng. Struct.* 132 (January) (2017) 70–86, <https://doi.org/10.1016/j.engstruct.2016.11.022>.
- [58] SR EN 12390-1-4:2002. Testing hardened concrete – Parts 1–4; 2002.
- [59] SR EN 10002-1:2002. Metallic materials – Tensile testing – Part 1: Method of test at ambient temperature, 2002.
- [60] S. Dudziak, W. Jackiewicz-Rek, Z. Kozyra, On the calibration of a numerical model for concrete-to-concrete interface, *Materials* 14 (2021) 7204, <https://doi.org/10.3390/ma14237204>.
- [61] W.V. Silva, L.M. Bezerra, C.S. Freitas, J. Bonilla, R. Silva, Use of natural fiber and recyclable materials for spacers in typical space truss connections, *J. Struct. Eng.* 147 (8) (2021), 04021112, [https://doi.org/10.1061/\(ASCE\)ST.1943-541X.0003018](https://doi.org/10.1061/(ASCE)ST.1943-541X.0003018).
- [62] Z. Hu, Y.I. Shah, P. Yao, Experimental and numerical study on interface bond strength and anchorage performance of steel bars within prefabricated concrete, *Materials* 14 (2021) 3713, <https://doi.org/10.3390/ma14133713>.
- [63] M. Yu, G. Wu, L. Kong, Y. Tang, Tire-pavement friction characteristics with elastic properties of asphalt pavements, *Appl. Sci.* 7 (2017) 1123, <https://doi.org/10.3390/app7111123>.
- [64] M. Koishi, K. Kabe, M. Shiratori, Tire cornering simulation using explicit finite element analysis code, *J. Appl. Polym. Sci.* 78 (2000) 1566–1572, <https://doi.org/10.1002/polb.10136>.
- [65] P. Desnerck, J.M. Lees, C.T. Morley, Strut-and-tie models for deteriorated reinforced concrete half-joints, *Eng. Struct.* 161 (2018) 41–54, <https://doi.org/10.1016/j.engstruct.2018.01.013>.
- [66] ABNT NBR 7188; Cargas móveis em pontes Rodoviárias. Associação Brasileira de Normas Técnicas, Rio de Janeiro, Brazil, 1982.
- [67] M. Gajewski, R. Szczepa, S. Jemiolo, Modelling of elastomeric bearings with application of yeoh hyperelastic material model, *Proc. Eng.* 111 (2015) 220–227, <https://doi.org/10.1016/j.proeng.2015.07.080>.
- [68] R.W. Clough, J. Penzien, Dynamics of structures, *Computers & Structures Inc., Berkeley, CA*, 1995.
- [69] Y.-Y. Lin, E. Miranda, K.-C. Chang, Evaluation of damping reduction factors for estimating elastic response of structures with high damping, *Earthq. Eng. Struct. Dyn.* 34 (11) (2005) 1427–1443, <https://doi.org/10.1002/eqe.499>.
- [70] B.E. Sobrinho, G. Gomes, W.V. da Silva, R. Silva, E.U. Palechor, L.M. Bezerra (Eds.), Differential evolution algorithm for identification of structural damage in steel beams, *Frattura ed Integrità Strutturale* 14 (52) (2020) 51–66, <https://doi.org/10.3221/IGF-ESIS.52.05>.
- [71] R. Silva, E.U.L. Palechor, L.M. Bezerra, M.V.G. de (Eds.), Morais, W.V. da Silva, Damage detection in a reinforced concrete bridge applying wavelet transform in experimental and numerical data, *Frattura ed Integrità Strutturale* 13 (48) (2019) 693–705, <https://doi.org/10.3221/IGF-ESIS.48.65>.
- [72] H.S. Ward, Traffic generated vibrations and bridge integrity, *J. Struct. Eng.* 110 (10) (1984) 2487–2498, [https://doi.org/10.1061/\(ASCE\)0733-9445\(1984\)110:10\(2487\)](https://doi.org/10.1061/(ASCE)0733-9445(1984)110:10(2487)).
- [73] A. Furtado, H. Rodrigues, A. Arêde, H. Varum, Modal identification of infill masonry walls with different characteristics, *Eng. Struct.* 145 (2017) 118–134, <https://doi.org/10.1016/j.engstruct.2017.05.003>.
- [74] A. Cunha, E. Caetano, F. Magalhães, C. Moutinho, Recent perspectives in dynamic testing and monitoring of bridges, *Struct. Control Health Monit.* 20 (6) (2012) 853–877, <https://doi.org/10.1002/stc.1516>.
- [75] A. Furtado, N. Vila-Pouca, H. Varum, A. Arêde, Study of the seismic response on the infill masonry walls of a 15-storey reinforced concrete structure in Nepal, *Buildings* 2019 (9) (2019) 39, <https://doi.org/10.3390/buildings9020039>.
- [76] P.-F. Li, Y.-F. Wang, B.-D. Liu, L. Su, Damping properties of highway bridges in China, *J. Bridg. Eng.* 19 (5) (2014) 04014005, [https://doi.org/10.1061/\(ASCE\)BE.1943-5592.0000578](https://doi.org/10.1061/(ASCE)BE.1943-5592.0000578).
- [77] H. Bachmann, W.J. Ammann, F. Deischl, J. Eisenmann, I. Floegl, G.H. Hirsch, G. K. Klein, G.J. Lande, O. Mahrenholtz, H.G. Natke, H. Nussbaumer, A.J. Pretlove, J. H. Rainer, E.-U. Saemann, L. Steinbeisser (Eds.), *Vibration Problems in Structures*, Birkhäuser Basel, Basel, 1995.
- [78] O. Poddavaeva, A. Fedosova, Damping capacity of materials and its effect on the dynamic behavior of structures. Review, *Energy Reports Volume 7 (Supplement 5)* (2021) 299–307, <https://doi.org/10.1016/j.egyr.2021.07.119>.
- [79] R.C. Battista, M.S. Pfeil, Bridge dynamics and aerodynamics: design and practical requirements for high structural performance and safety, *Struct. Infrastruct. Eng.* 14 (4) (2017) 491–508, <https://doi.org/10.1080/15732479.2017.1406962>.
- [80] F. Gong, F. Han, Y. Wang, Y. Xia, Bridge damping extraction method from vehicle-bridge interaction system using double-beam model, *Appl. Sci.* 11 (2021) 10304, <https://doi.org/10.3390/app112110304>.
- [81] M.H. Rahman, C. Gupta, Computation of Rayleigh damping coefficient of a rectangular submerged floating tunnel (SFT), *SN Appl. Sci.* 2 (2020) 936, <https://doi.org/10.1007/s42452-020-2629-z>.
- [82] N.S. Idris, K.H. Boon, A.F. Kamarudin, S.Z. Sooria, N. Abd Rahman, Z. Mohd Jaini, R. Yunus, S.N. Rahmat, Ambient vibration test on reinforced concrete bridges, *MATEC Web Conf.* 47 (2016) 02012.
- [83] H. Bachmann, W. Ammann, *Vibrations in structures—Induced by man and machines*, SED 3 (1987) IABSE.
- [84] C.W. Lin, Y.B. Yang, Use of a passing vehicle to scan the fundamental bridge frequencies: An experimental verification, *Eng. Struct.* 27 (13) (2005) 1865–1878, <https://doi.org/10.1016/j.engstruct.2005.06.016>.
- [85] J.Y. Moreno-Martínez, R. Meli, Experimental study on the structural behavior of concrete dapped-end beams, *Eng. Struct.* 75 (2014) 152–163, <https://doi.org/10.1016/j.engstruct.2014.05.051>.